PPPL-2103 DR-1020-0 PPPL-2103

UC20-A I-21081

SEMIEMPIRICAL MODELS OF H-MODE DISCHARGES

By

C.E. Singer et al.

MAY 1985

PLASMA
PHYSICS
LABORATORY

PRINCETON UNIVERSITY
PRINCETON, NEW JERSEY

PREPARED FOR THE U.S. DEPARTMENT OF ENERGY,
UNDER CONTRACT DE-AC02-76-CHO-3073.

PPPL--2103

DE85 011581

SEMIEMPIRICAL MODELS OF H-MODE DISCHARGES

C. E. Singer, M. Redi, D. Boyd, A. Cavallo, B. Grek, D. Heifetz, R. Hulse,
D. Johnson, W. Langer, B. LeBlanc, D. Mikkelsen, and F. Seidl
Plasma Physics Laboratory, Princeton University
Princeton, New Jersey 08544

and

A. Eberhagen, O. Gehre, F. Karger, M. Keilhacker, S. Kissel, O. Klüber,
D. Meisel, H. D. Murmann, H. Niedermeyer, H. Rapp, H. Rohr, A. Stäbler,
K. H. Steuer, and F. Wagner
Max Planck Institut für Plasmaphysik
D-8046 Garching bei München
Federal Republic of Germany

531 3000

[illegible] 7566

ABSTRACT

The H-mode transition can lead to a rapid increase in tokamak plasma confinement. A semiempirical transport model was derived from global OH and L-mode confinement scalings and then applied to simulation of H-mode discharges. The radial diffusivities in the model also depend on local density and pressure gradients and satisfy an appropriate dimensional constraint. Examples are shown of the application of this and similar models to the detailed simulation of two discharges which exhibit an H-mode transition. The models reproduce essential features of plasma confinement in the ohmic heating, low and high confinement phases of these discharges. In particular, the evolution of plasma energy content through the H-mode transition can be reproduced without any sudden or ad hoc modification of the plasma transport formulation.

1. INTRODUCTION

The H-mode transition is a rapid change in the peripheral plasma in a tokamak. This rearrangement is often associated with a significant increase in global electron energy and particle confinement. The changes in plasma profiles which accompany the H-mode transition provide one of the severest tests of any quantitative description of plasma transport which can be cast in the form of a transport simulation. In this regard, the present paper has two purposes. First, we present examples of how theoretical hypotheses about driving forces for turbulence and dimensional constraints can be incorporated into otherwise empirical transport models. We also illustrate the use of an improved scrape-off plasma model. Second, we present two rather complete data sets from divertor tokamaks in a form which should be useful for calibrating future transport simulation models. Since complete data sets for single discharge sequences are only rarely reported in a form useful for supporting comprehensive modeling exercises, the present paper should provide a useful reference for transport modelers. To these ends, we concentrate on the rationale behind the construction of a semiempirical transport model, and we use the results as a framework for presenting the two data sets in detail. Since our baseline semiempirical model is not the only model which reproduces these data sets, we also present other models which fit the data. The modeling results support only very limited and tentative conclusions about the nature of the transport processes in H-mode plasmas. Nevertheless, we believe that working through the motivation and application of the two example semiempirical calculations presented here may provide some insight into possible plasma transport processes in H-mode discharges.

We now review some major features of the H-mode transition and how our simulations were designed around these features. Observations of the H-mode plasmas [1-9] can show changes in two distinct regions of the poloidal cross sections of diverted tokamaks shown in Figs. 1 and 2. First, the core plasma can develop broad density and temperature profiles. Large increases in density and temperature have also been observed at the transition on the midplane, on the outer uninterrupted magnetic flux surfaces (inside the inner solid curve on Fig. 1). There is therefore empirical motivation for modeling possible effects of changing profile shapes on plasma transport. Below we outline the theoretical motivation for such models, and we illustrate how broadening of density and pressure profiles may contribute to good energy confinement in the H-mode, at least in PDX.

The formation of the H-mode can also be accompanied by substantial changes in plasma parameters in and near the divertor chamber. In particular, a noticeable drop in the H_α emission near the divertor plate is often taken as an operational definition of the H-mode. A reduction of the electron temperature is sometimes also clearly seen to develop in the divertor at the separatrix during the H-mode [5,6]. This drop in T_e suggests the development of a cooler high-recycling divertor (sometimes associated with high confinement [3,9]). Since previous models of the scrape-off plasma in our simulation code were not designed for modeling of a high-recycling divertor, we included a new "two-chamber" model [7] of flows along magnetic field lines, as described in Sec. 3 and the Appendix.

We now describe the semiempirical transport and boundary plasma model in detail, show to what extent it can describe core-plasma energy confinement, illustrate how the model thermal diffusivities vary during the evolution of a discharge, and discuss which properties of the model are pertinent to obtaining an H-mode transition. The overall physics of the core plasma and divertor models are described in the next two sections. The specific parameters of the model are then described, followed by the results for PDX and ASDEX with discussion and conclusions. Numerical details are discussed in the Appendix.

2. RADIAL PLASMA TRANSPORT

To understand transport phenomena in tokamaks, it is probably essential to consider the dependence of transport coefficients on profiles of plasma parameters. This is clear from the theories of drift [10] and rippling modes [11] which depend at least on density and temperature gradients, and from the theory of resistive ballooning modes [12] where pressure gradients and magnetic shear play an important role. These so-called profile effects have been omitted in most previous simulations and data analysis, as their inclusion requires overcoming various conceptual and numerical difficulties.

To illustrate how we incorporate profile factors into thermal and particle diffusivities and pinch flows, we present a baseline example calculated with circular flux surfaces. First, we write the plasma transport equations, then the general form used for transport coefficients, and finally, the specific transport coefficients used in the present application. The plasma transport equations are [13-16]

$$\frac{\partial}{\partial t}\left(\frac{3}{2}n_j T_j\right) = \frac{1}{r}\frac{\partial}{\partial r}\left(r n_j \chi_j \frac{\partial T_j}{\partial r} - r Q_j^{conv}\right) + W_j - Q_j/L_{\parallel} \; ; \; j = i,e \tag{1}$$

$$\frac{\partial n_a}{\partial t} = -\frac{1}{r}\frac{\partial}{\partial r}\left(r\Gamma_a\right) + S_a - n_a/\tau_{\parallel} \; , \; a = H,D,O,Fe \tag{2}$$

$$\frac{\partial}{\partial t}(rB_\theta) = \frac{c^2}{4\pi} r \frac{\partial}{\partial r}\left[\frac{\eta}{r}\frac{\partial}{\partial r}(rB_\theta)\right] - 2\pi r \frac{\partial}{\partial r}\left(\eta J_{beam}\right) \; , \tag{3}$$

where T_e, T_i, n_e, and $n_i = \sum_a n_a$ are the thermal electron and ion temperatures and densities, W_j, S_a, and J_{beam} are sources related to ohmic heating, neutral beam injection, coulomb ion-electron energy exchange, radiation, charge exchange, and ionization. B_θ is the poloidal magnetic field, and η is the neoclassical parallel resistivity [15], and r is the (poloidally averaged) minor radius. The scrape-off losses, $Q_j/L_\parallel$ and $n_a/\tau_\parallel$ are defined below. Following a common type of convention, we set the convective heat losses $Q_j^{conv} = 2.5\ \Gamma_j T_j$ where $\Gamma_i = \sum_a \Gamma_a$ and Γ_e is determined by quasineutrality [16,17]. The remaining anomalous transport is incorporated into flexible expressions for the electron thermal diffusivity

$$\chi_e = \sum_n \chi_n^* \prod_k X_k^{e_{nk}} ,$$

and the particle flux for each species

$$\Gamma_a = -D_a \frac{\partial n_a}{\partial r} - n_a v_a , \tag{4}$$

$$D_a = \sum_n D_{a,n}^* \prod_k X_k^{d_{nk}} , \tag{5}$$

$$v_a = v_a^{Neoclassical} + \sum_n v_{a,n}^* \prod_k X_k^{f_{nk}} . \tag{6}$$

Here the X_k are suitable dimensionless scaling parameters described below, and the associated scaling exponents are primarily determined from global empirical confinement data and constrained to be dimensionally consistent with the collisional Vlasov equations [14,18,19,20].

The essential problem in semiempirical transport modeling is to pick the smallest set of dimensionless scaling parameters which can reasonably be expected to reflect the underlying transport physics [13]. We posit that the smallest such set contains the plasma β, the collisionality, the ratio ρ_L/r of the gyroradius to a locally determined size parameter, the safety factor q, the inverse aspect ratio ε, a measure $\lambda_p = (r/p)dp/dr$ of the pressure gradients which drive kinetic ballooning, the magnetic shear which acts primarily to stabilize the pressure-driven modes [12], a measure $\lambda_n = (r/n)dn/dr$ of the density gradients which are particularly important for driving microinstabilities at low β, and a measure $\lambda_{Te} = (r/T_e)dT_e/dr$ of the temperature gradients which affect the stability [12]. Note that the transport is assumed to be independent of the ratio λ_{Debye}/r of the Debye length to size; this assumption provides an invaluable dimensional constraint on $\chi_e(r)$ [18,19].

We start the construction of our thermal diffusivity with a density-gradient driven term, χ_n, which dominates energy confinement in low-β plasmas, where the pressure gradient is small. Using the estimate $\tau_E \propto r^2/\chi_n$, this term is constrained to have the same parameter scaling as the Pfeiffer-Waltz scaling for electron energy confinement [20]. For the unknown temperature dependence in this ohmic confinement scaling [20], we assume a favorable confinement scaling with temperature, $\chi_e \propto T_e^{-0.5}$, as perhaps suggested by early studies of the radial dependence of χ_e in ohmic discharges [21]. This χ_n term is only important to H-mode studies in the outer half of the discharge, where the usual negative temperature gradient may be stabilizing [10]. This simple model therefore has larger values of $|\lambda_{Te}|$ stabilizing χ_n, which is adequate for the studies at hand.

We also add a pressure-gradient driven, shear-stabilized diffusivity χ_{aux} [12]. Using the estimate $\tau_E \propto r^2/\chi_{aux}$, this term is constrained by the scaling of global energy confinement data for τ_E for beam-heated L-mode tokamaks as presented at the 1982 IAEA meeting in Baltimore [1,23-25]. The two sawteeth which occur in the ASDEX L-phase of beam heating are treated with a model which flattens profiles and conserves helical flux [22]. For the high frequency of sawteeth in the ohmic phase this is numerically inconvenient and unnecessary, so particle and electron thermal diffusivities are instead continuously enhanced inside the $q \sim 1$ surface. (In the beam-heated plasmas, the enhancement used here for $q \lesssim 1$ is very small and serves here only to avoid a numerical singularity on axis.)

Thus, the scaling exponents of all but the profile factors $\lambda_X = (r/X)dX/dr$ and $\chi_{aux}(\varepsilon)$ are determined by previous dimensionally constrained observations of OH and beam-heated plasmas. But only the signs of the scaling exponents of the profile factors are so determined, here by theoretical considerations described above. We also had some freedom in choosing the $\chi_n \propto T_e^{-1/2}$ scaling exponent for the term dominant during ohmic heating. It is therefore not surprising that such a model has the flexibility to reproduce both the observed profile shapes and degradation of confinement between OH- and L-mode plasmas observed in the ASDEX example discussed below. It is not immediately obvious that such a model can reproduce the confinement observed in the ASDEX and PDX H-modes. To see how such a model can succeed in doing this, we now describe a specific model used to fit PDX and ASDEX discharges. We start with the specific scrape-off plasma model used and then proceed to give the precise parameters used to define the radial transport coefficients.

3. DIVERTOR PLUGGING AND RECYCLING

A major problem in transport simulation of divertors is to find a computationally practical model in which the plasma responds in a physically reasonable manner to changes in divertor plugging [7]. We now describe the dominant physical processes in the plasma scrapeoff and how we constructed a simple model of them. Changes in the divertor plasma affect both loss of plasma along magnetic flux surfaces and recycling of neutrals. In particular, ionization dilutes the plasma momentum influx and slows the flow of plasma along magnetic field lines from the main plasma chamber. This effect is included in our transport simulations using poloidally averaged sink terms $-n_a/\tau_\parallel$ for the ion densities, n_a, in the main chamber scrapeoff. Here $\tau_\parallel = Mv_s/L_\parallel$, v_s and $L_\parallel$ are the sound speed and parallel connection length defined in the Appendix, and M is the Mach number for flow along field lines from the main plasma chamber. This parallel Mach number can be related to the fraction α of the recycling neutrals which are ionized in the divertor throat. A simple analysis of the continuity equations along open field lines [7,15] gives $M = [(\alpha/2)(T_e/T_{div})^{1/2}]$. Here $\alpha = 1 - (1 - f_{leak})[1 - \exp(-L_{div}/\lambda^o_{mfp})]$ is the fraction of recycling neutrals ionized in the divertor chamber (i.e., the "plugging fraction"). The neutral mean-free path is $\lambda^o_{mfp} = v_o/(n_{div}\langle\sigma v\rangle_{div})$ where $v_o = \xi(2E_o/\bar{m}_o)^{1/2}$, and $\bar{m}_o$ is the mean neutral mass. L_{div} is the approximate neutral path length from the divertor plate to the main plasma chamber, ξ is a geometric factor to account for the zig-zag neutral trajectory through the divertor throat, E_o is a neutral energy (set to a constant value near the density-weighted volume average divertor temperature $\langle T_{div}\rangle_n$), and f_{leak} is the fraction of neutrals which enter the main plasma without passing through the divertor throat. The parameters L_{div} = 40 cm, ξ = 0.5, and f_{leak} = 0.05 are roughly estimated from the divertor geometries and kept constant in each simulation, and the plugging fraction and parallel Mach number evolve in response to changing plasma conditions. The divertor density evolves according to the approximate pressure balance along the magnetic field lines, $n_{div}(r,t) = n_eT_e/(2T_{div})$ where n_e and T_e are the midplane electron density and temperature computed by evolving the one-dimensional radial transport equations described above. We compute $T_{div}(r,t)$ from the parallel energy balance, as described in the Appendix. The total electron impact ionization rate coefficient $\langle \sigma v \rangle_{div}$, was computed from T_{div} using the formula of Freeman and Jones [27]. There was also a loss of electron and ion energy from the midplane scrapeoff by flow along magnetic field lines to the divertor chamber, as described in the Appendix. This and the above-mentioned particle losses represent the only direct effects of the computed divertor parameters (n_{div} and T_{div}) in our model. However, the computed temporal evolution of T_{div} is a useful diagnostic which can be conceptually related to changes in recycling at the divertor plate [28,29].

The action of the divertor model in our simulations was as follows. With the high divertor pressure at the H-mode transition in the ASDEX simulations detailed below, the transition gave a reduction in the particle outflux, as postulated elsewhere [6]. An increase in the divertor throat opacity also contributed to maintenance of good confinement by blocking particle outflow along open field lines and flattening the electron density profile. With the lower divertor pressure in the PDX simulation, formation of the H-mode was instead driven largely by changes in electron density profiles reproduced by a modest increase in the neutral gas density. This would be consistent with an increase in divertor recycling, as in an earlier speculation [8]. A synthesis of previous viewpoints (cf. [6,8]) on the role of the scrapeoff in the H-mode transition has thus been approached in our modeling.

4. MODELING PARAMETERS

A complete description of the H-mode transition evidently requires a detailed understanding of the poloidally asymmetric flows of plasma and neutral gas in the divertor and main plasma chambers. Complete computational models of these flows have yet to be fully extended to this complicated geometry. Nevertheless, insight can be gained by using the following model of the poloidally averaged plasma flows.

4.1 Electron thermal diffusion coefficients

The standard formulation used here for the electron thermal diffusivity was

$$\chi_e = \chi_{aux} + \chi_{OH} \ . \tag{7}$$

Expressed with convenient dimensional variables, the thermal diffusivities were

$$\chi_{aux} = 6 \times 10^3 \left(\frac{p}{p_*}\right)^{1.0} \left(\frac{n_e}{n_*}\right)^{-0.2} \left(\frac{r}{r_*}\right)^{0.4} \left(\frac{B}{B_*}\right)^{-2.0} \left(\frac{q}{1.5}\right)^{2.2} \left(\frac{\varepsilon}{0.14}\right) \frac{|\lambda_p|}{2.0} \left(\frac{|\lambda_q|}{0.6}\right)^{-2} , \tag{8}$$

$$\chi_{OH} = \chi_n + \chi_q \ , \tag{9}$$

where

$$\chi_n = \chi_o \left(\frac{|\lambda_n|}{0.9}\right)^{1/2} \left(\frac{|\lambda_{Te}^+|}{1.0}\right)^{-1/2} , \tag{10}$$

$$\chi_q = \chi_o \, q^{-10} \, (\varepsilon/0.14)^{-1.1} , \tag{11}$$

and

$$\chi_o = 6\times10^3\left(\frac{n_e}{n_*}\right)^{-0.9}\left(\frac{r}{r_*}\right)^{-1.0}\left(\frac{\epsilon}{0.14}\right)^{1.9}\left[\frac{T_e}{T_*}\left(\frac{B}{B_*}\right)^{-0.9}\left(\frac{r}{r_*}\right)^{-0.4}\left(\frac{q}{1.5}\right)^{0.8}\left(\frac{Z_{eff}}{3.0}\right)^{-0.5}\right]^{-0.5} . \tag{12}$$

(Here $p = n_iT_i + n_eT_e$, $\epsilon = r/R$, and r is average minor radius of a magnetic flux surface. The normalization constants $p_* = 4.3 \times 10^{13}$ keV/cm^3, $n_* = 2.2 \times 10^{13}$cm^{-3}, $r_* = 20$ cm, $B_* = 1.7$ T, and $T_* = 1.1$ keV, and the denominators of the above λ factors are typical parameter values, e.g., for the low confinement phase (L-mode) at r = 20 cm of the PDX discharge discussed in detail below. (Gaussian units are used except in the formulas which include these normalization parameters.) Singularities on axis are avoided by adding the fractional width of the innermost computational zone to form $|\lambda^+_{Te}| = |\lambda_{Te}| + 0.06$. χ_e is also limited to be no greater than about Bohm diffusion near the scrapeoff, as described in the Appendix.

This model produces improved confinement at higher pressure in the H-mode, despite the fact that the pressure-driven term dominates the inner plasma in L-mode discharges in the model. There are two reasons for this. First, the $\chi_{OH} \propto n_e^{-0.9}T_e^{-0.5}$ scaling allows good edge confinement at high edge density and temperature, thereby reinforcing the H-mode at high edge pressures. The high-density contribution to this effect is very pronounced in the PDX simulation described below. (Note the sensitive dependence of edge confinement on the χ_{OH} term. Deep fueling and/or edge cooling should reduce n_e and/or T_e [8] and tend to "flip" the model back into the L-mode.) Second, there is a small stabilized region of high shear near the separatrix. Broadening the pressure profiles allows a large pressure gradient to occur in this shear-stabilized region.

4.2. Other simulation parameters

The standard energy transport equations used $\chi_i = 3\chi_i^{CH}$ where χ_i^{CH} is the formula of Chang and Hinton [15,31,32] scaled with Z_{eff} as described in the Appendix, classical electron-ion coulomb energy interchange, ohmic electron heating, a multigroup Fokker-Planck model of heating by neutral beams, and (for PDX) coronal equilibrium radiation from oxygen and iron impurities [15,33]. The radial fluxes of oxygen, iron, hydrogen, and/or deuterium were given by

$$\Gamma_a = -D_a \frac{\partial n_a}{\partial r} - n_a v_a \; ,$$

where $D_a = 0.2\chi_e$. The impurity pinch included neoclassical bulk frictional drag effects [15] and an anomalous pinch $v_a = -1.2\ D_a \partial \ell n_e / \partial r$, compatible with recent theory and measurements of transport rates during impurity injection experiments [8,34,35]. *Our standard model uses only the Ware pinch for* hydrogen isotopes [15]. This is adequate, with our other transport coefficients, to reproduce the density rise observed by Strachan *et al.* on PLT [36].

5. PDX

5.1 Forced constraints on the simulation

The PDX discharge had major radius R = 140 cm, separatrix mean minor radius $r_{sep} = 40 \pm 1.5$ cm [9], and toroidal magnetic field B = 17 kG. The toroidal plasma current is shown for the PDX case in Fig. 3. This current was used to determine the outer boundary condition on the poloidal flux equation, Eq. (3).

Feedback control of a neutral gas influx at $v_o = 0.5\ (2E_o/m_o)^{1/2}$ was used in the simulation to match the observed line-integral electron density. Monte Carlo neutrals were initially launched radially inwards onto a simple circular cylindrical plasma, so the resemblance to the actual divertor configuration is only heuristic, as noted above. As in the divertor chamber model described above, we chose E_o to be a constant typical of the divertor temperature (8 eV, except for the pretransition PDX plasma, where $\langle T_{div} \rangle_n \approx E_o = 60$ eV, cf. below). Note the important factor of $\xi \approx 0.5$ in this version of v_o to account for the expanded magnetic geometry near the x-point where most neutrals enter the core plasma.

The evolution of the line-average density is shown in Fig. 3. In the experiment, this was achieved using a constant gas puffing rate of 20-30 torr-liters D_2 per second. To match the rapid increase in line-average density at the H-mode transition for this PDX case required an abrupt 3%/msec increase in the total neutral gas <u>reflux</u> rate (gas puffing <u>plus</u> recycling) in the simulation. It is interesting to note that divertor chamber temperature, $\langle T_{div} \rangle_n$ estimated by the simulation as described above, abruptly decreased from 60 eV before the transition to 8 eV within less than 5 msec after the transition in the PDX simulation. Recent examinations of the energy dependence of particle reflection coefficients from a metal plate suggests a significant decrease in surface sticking may occur when the plasma temperature drops through a value roughly estimated to be in the range of 5-10 eV [29,30]. Such a drop in the divertor temperature should therefore produce an increase in the total neutral gas reflux. These considerations suggest that we may have a qualitatively self-consistent picture of changes in plasma recycling for this particular H-mode transition, but they certainly do not rule out alternative explanations such as an abrupt improvement in particle confinement.

The total influx of impurities was adjusted to match approximately the evolution of Z_{eff} measured by observations of visible Bremsstrahlung, as shown in Fig. 4. Impurity radiation accounts for a maximum of 0.1 MW of the simulated bolometer signal (compared to data in Fig. 5); the remainder of the bolometer signal in the simulation is due to neutral particle outflux.

2.2 MW of D_o was injected into a D^+ plasma at a mean tangency major radius R_{tang} = 34 cm from t = 0.3 s to t = 0.6 s (with 1.8 MW at 44 keV, 0.3 MW at 22 keV, and 0.1 MW at 15 keV). Fishbone events produced an approximately constant time averaged fractional neutron production loss of about 15% in the L-mode phase, with the loss dropping to a much smaller value in the H-phase, as shown in Fig. 6. This fast ion loss was neglected in our baseline simulation. Including this loss had almost negligible effect on the simulation, as discussed below in Sec. 5.2.

5.2 Results

The above model reproduced the flux surface averages of n_e, T_e, central T_i, β_T, and $\Lambda = \beta_p + \ell_i/2$ within the absolute calibration and shot-to-shot variation of the experimental data, as illustrated in Figs. 7-10. Of particular interest is the simulated increase of density and temperature through most of the plasma in the H-mode. There are, however, two possible discrepancies which lie within the absolute calibration limits, but which are nevertheless discernable from the relative change in the temporal evolution of channels shown in Fig. 9. In particular, the simulated drop in central ion temperature around t = 0.45 s is comparable to uncertainties in the concomitant 36% increase in n_i/n_e, dependent on the mix of heavy and light impurities in the discharge. We therefore do not know the ion density well enough to simulate the ion temperature around t = 0.45 s to better than this accuracy.

A more interesting problem is that the simulation underestimates the L → H rise in T_e at R = 176 cm. Individual variation of almost all the adjustable parameters in our model has failed to reproduce this T_e rise. It would be tempting to conclude that this implies an abrupt change in the thermal conduction mechanism at this radius. Without calibration of temperature, density, and fueling profiles to much better than this accuracy, further progress on this problem is impractical.

The above uncertainties about peripheral plasma transport are not necessarily critical for the global confinement transition simulated for PDX. To demonstrate this point, we made significant alterations in the edge plasma transport model and yet found the core plasma parameters were only slightly affected. In particular, we performed a simulation with an ad hoc decrease from the nominal value 6×10^3 of the leading coefficient (c_n) in the edge-dominant term, χ_n. This change gave $d\ell nT_e/d\ell nc_n = -0.38$ at R = 176 cm and t = 0.6 s, but a much smaller $d\ell n\langle\beta_T\rangle/d\ell nc_n = -0.03$ (where $\langle\beta_T\rangle$ is the volume average toroidal β). This result demonstrates that the global confinement transition is not necessarily dependent on exact details of the edge profiles (provided the edge is opaque to neutrals, cf. below). That global confinement is not a simple function of edge temperature is also supported by statistical studies of the edge temperature in PDX L → H transitions [9] which show H-mode transitions at various values of edge T_e. This conclusion is also consistent with transport analysis [17] results which show a decrease in χ_e throughout the q > 1 region of the plasma as a result of the L → H transition, not just at the plasma edge [3].

Two other peculiarities of the PDX simulation are worth comment before proceeding to the ASDEX case. First, the fishbone-induced loss of injected fast ions mentioned above seems not to be a significant factor in the transition. With a 15% fishbone reduction of the 44 keV injection power from t = 413 ms to 534 ms (cf. Fig. 6), the simulated L-mode $\langle\beta_T\rangle$ is lower by only one part in 20, as shown by the lower smooth solid curve in Fig. 10. (This does not preclude the possibility of fishbone effects on transport of thermalized plasma.)

Second and more interesting, the rapid density rise in our PDX simulation produces a significant drop in the estimated divertor temperature (an effect sometimes also observed with divertor chamber probes near the separatrix on PDX). There is likely to be some concomitant rapid change in divertor recycling. However, this change may not exactly correspond to the 60 → 8 eV reduction of incoming neutral velocity at the L → H transition in our baseline PDX simulation. We therefore tried an additional simulation with a constant E_o = 8 eV for recycling neutrals instead of $E_o \approx \langle T_{div}\rangle_n$ as in the standard stimulation. An L → H transition was still obtained in this case. But the pretransition $\langle\beta_T\rangle$ was much larger than in the standard simulation, as shown in Fig. 10. This remarkable sensitivity to changing fueling and density profiles is one of the major results of our modeling. This result suggests that further study of such discharges should concentrate on obtaining accurate fueling and density profiles.

5.3. Global Energy Confinement

The most fundamental measure of the energy confinement transition is the evolution of stored energy in the plasma. In Fig. 10, we compare measurements of β_T (from the diamagnetic loops) and $\Lambda = \beta_p + \ell_i/2$ (from the equilibrium field) to the corresponding values computed [37] from the simulations (smooth solid curves). These comparisons clearly show an increase in the rise of plasma stored energy well into the beam-heating portion of the discharge at the L→H transition. This increase in stored energy occurred much later than a global energy confinement time for the L-mode phase, which was 22 ms at t = 0.52 s in the PDX simulation (and increased to 39 ms at t = 0.60 s in the H-mode phase). This is the essential feature of interest in these simulations (cf. Sec. 7).

6. ASDEX

We have also modeled a well-documented ASDEX H-mode discharge, with the following machine parameters: R = 164 cm, r_{sep} = 40 ± 1 cm, B = 22 kG, and 2.9 MW of $H^o \rightarrow D^+$ starting at t = 1.106 s (with half at tangency major radius R_{tang} = 130 cm and half at R_{tang} = 150 cm, and 1.6 MW at 40 keV, 0.8 MW at 20 keV, and 0.5 MW at 13 keV). The toroidal current was established at a constant value of 375 kA before t = 1.0 s and kept constant through the beam injection phase of the discharge. Unlike the PDX discharge described above, the midplane line-average density showed a smaller rise after the H-mode transition, as shown in Fig. 11. The timing of the H-mode transition is indicated by a sawtooth-induced small drop in $\bar{n}_e$ and a decline in the divertor H_α emission as indicated in Fig. 11. Similar discharges in this series have a sawtooth at the L → H transition with a drop of 0.20 keV in the central electron temperature, as in the simulation. An earlier sawtooth of much smaller amplitude is observed about 23 ms before the transition in similar discharges and is also explicitly included in the simulation.

6.1. Results

The simulated and measured density profiles are shown for the OH-, L-, and H-mode phases of the ASDEX case in Fig. 12. The Thomson scattering data may suggest slightly broader profiles than those calculated in the simulation in the L- and H-modes. However, the lower interferometer trace in Fig. 11 suggests more peaked density profiles than in the simulation. The simulated density profiles therefore may lie within the bounds of experimental error.

The electron temperature profiles generally lie within the experimental uncertainty of the cyclotron emission and Thomson scattering measurements as is evident in Fig. 13. In both the experiment and simulation, the increase in β_T and Λ, shown in Fig. 14, are more continuous than in the PDX case.

7. DISCUSSION

7.1. Factors controlling confinement

To illustrate where the pressure and density-gradient-driven contributions to our model have their effects, we have plotted in Fig. 15 contributions to the thermal diffusivities for the discharges described above. The decrease in global energy confinement between OH- and L-modes in this model results from two causes. First, there is an outward shift of the heating profiles (the half-width of the heating profile shifting outward by 50% in PDX upon application of beam heating). Second, there is the additional pressure-gradient-driven contribution in the beam-heated plasma (cf. Fig. 15).

The good energy confinement, which occurs after the L → H-mode transition, is allowed to be obtained in our model by suppression of the dominant χ_{OH} contribution in the outer part of the plasma due to the increase in edge n_e in PDX, as illustrated in Fig. 15a. Also, there is a relatively small increase in the χ_{aux} contribution despite the higher absolute pressure.

7.2 Time scale for the L→H transition

The type of transport models proposed in this paper have transport coefficients which are smooth functions of local plasma parameters. In such models, changes in local plasma parameters can occur on the local time scales for fueling, heating, and poloidal flux diffusion. We hypothesize that some such model can describe all plasma properties not directly correlated with large scale MHD activity. If this hypothesis is correct, then faster jumps in T_e associated with H-mode formation should always be partly due to MHD activity. An exhaustive analysis of whether or not this hypothesis is true is not available. In particular, it is known that H_α discontinuities occur in the absence of significant core-plasma temperature oscillations; but this observation alone does not answer the question of whether the larger temperature jumps and/or the rapidity of changes in plasma confinement may be partly due to changes in observable MHD activity or changes in magnetic island structures. *All that is presently known is that MHD activity can affect the* time scale for formation of the H-mode, particularly in sawtooth discharges. The rapid broadening of density and temperature profiles following a sawtooth can throw the discharge into the H-mode in 0.3 msec or less, as illustrated previously in a simpler simulation model [8]. However, that the H-mode has been achieved is clear from electron cyclotron measurements only after 2-3 msec beyond the sawtooth which induces the H-mode, as indicated by failure of T_e to decline at $r \approx 30$ cm. In the absence of fishbone and sawtooth oscillations, the transition requires 2-3 msec, which is the time scale for fueling and thermal inertia in the outer 10 cm of the core plasma in our PDX simulation. All of the above comments are compatible with the idea that the transition merely involves a gradual (2-3 msec) broadening of the profiles in this region, accompanied by changes in the scrapeoff and followed by changes deeper in the core plasma.

7.3 Comparison with empirical transport model results

There may also be some insight to be gained by comparing the transport coefficients in our model to those deduced from other local energy transport analyses of PDX and ASDEX, since these analyses should contain additional information on radial variations--information not directly included in the global energy confinement scalings used to constrain our thermal diffusivities. A comparison has been made with the χ_e from the TRANSP code [17], deduced by starting from the observational data and inverting Eq. (1) for the present PDX case [9]. This comparison showed a larger value of χ_e around r = 27 cm from TRANSP than in our simulations. Much of the difference is accounted for by the different methods used to estimate the poloidally averaged neutral density and the ion energy transport.

We have also checked the χ_e computed from our Eqs. (7) to (12) for the beam-heated portion of a high-density $H^o \rightarrow D^+$ L-mode discharge against that computed from the data analysis code, TRANSP. This high density case was chosen because the onset of H-mode confinement in our PDX simulation is due to suppression of the χ_{OH} term, which has a strong density dependence. It was found that the χ_e computed in the "confinement region" at r = 25±10 cm from our formula was proportional to that from TRANSP and lay approximately within the error limits of the TRANSP analysis, and showed a strong radial rise in the outer half of the discharge. This poor peripheral confinement in our formula was due primarily to the low electron temperature [cf. Eq. (12) above].

We have also made a qualitative comparison of the compatibility of our transport model with the conclusions drawn by Becker et al. [38] from simulation of L- and H-mode discharges from ASDEX. The model of Becker et al. replaced the ohmic transport coefficients by purely empirical enhancement terms (χ_{aux} and D_{aux}) turned on during various L- and H-mode regimes. The onset and disappearance of the enhanced losses were delayed with respect to turning on and off neutral beam heating. By way of comparison, the fixed semiempirical formula for χ used in the present work leads to global confinement with similar dependence on heating power to that required by Becker _et al_. Also, the full effect of our semiempirical χ_{aux} should be delayed by the thermal inertia of the plasma after the onset of auxiliary heating and by beam slowing-down and plasma energy confinement after the termination of auxiliary heating. A remarkable feature of the empirical model of Becker _et al_. is the long duration of the additional losses in the L-mode, these losses being retained up to 0.1 sec after cessation of neutral beam injection. Evolution to broader current profiles would tend to reduce the shear stabilization term in our model and persist for a poloidal-current-diffusion time after the cessation of beam heating, but it is not known whether this is sufficient to reproduce the delay effect noted by Becker _et al_.

7.4 Comparison with simpler transport models

The model proposed in Sec. 4.1 fits the experimental data satisfactorily and is based on theoretical concepts believed fundamental to a real understanding of microscopic plasma physics. However, several tests of this transport model show that certain features of the model are not necessary to simulate the PDX and ASDEX experiments presented here. These tests show that simpler models are adequate for predicting the plasma density and temperature profiles found in these experiments and that the evolution of the global energy confinement time from L- to H-mode is similar in all of the models.

Four transport models have been compared in this study. Model 1 is the baseline transport model of Sec. 4.1 and 4.2. The other models are simplifications of the formulas in the baseline model. The transport coefficients of Model 2 have no profile factors. Model 3 includes no χ_{aux}, D_{aux}, or v_{aux} terms. The transport coefficients of Model 4 have no χ_{aux}, D_{aux}, or v_{aux} and have only a $1/(n_e T_e^{1/2})$ variation in χ_n (cf. [43]) with D and v related to χ as for the baseline model in Sec. 4.2. All of these models have a strong radial dependence and a contribution to χ_e proportional to $1/(n_e T_e^{1/2})$. The magnitudes of the transport coefficients in simpler models have been adjusted in the simpler models to agree roughly with those of the baseline model midway into the confinement region between q = 1 and q = 2.

Figure 16 shows the temperature profiles for the PDX and ASDEX simulations for each of the models being tested as well as the experimental data points. It is clear that the data do not allow discrimination among the transport models. A modest increase in the magnitude of χ_e in Model 2 would decrease the central temperature, but, in fact, the results predicted by this model are not very different from those predicted by the other models. The electron density profiles predicted by the simplified models also agree with the baseline model predictions within the experimental error. All of the models produce the broadened H-mode density profile for PDX. All produce model plasmas which evolve from ohmic to L-mode to H-mode in agreement with the ECE and Thomson scattering data on temperature and density within the experimental error. The agreement can be further improved by adjusting the overall magnitude of the transport coefficients.

One significant measure of plasma energy confinement is the evolution of the stored energy in the plasma. BALDUR calculates the total energy confinement time as the total stored energy divided by the total plasma energy transport flux across the separatrix. In Table 1 is shown the global energy confinement time computed for the four transport models applied to the PDX and ASDEX experiments. Each model does predict an H-mode transition with H-mode confinement time about twice that of the L-mode confinement time for PDX. But none of these models, including the baseline model, simulates a large drop in PDX energy confinement time when the plasma passes from OH to L in contradiction to the trend observed in PDX limiter discharges at comparable current [44] and in "typical" PDX divertor discharges [9]. The global energy confinement times from the simulation of the ASDEX experiment for the transport models are also presented in Table 1. As for the PDX simulations, each model produces an increased confinement time at the L- to H-mode transition. The transport models without profile factor and with only the "ohmic" term show a drop in energy confinement time at the OH to L-mode transitions as does the baseline semiempirical transport model in agreement with the ASDEX experiments. Model 4 does not show an OH to L transition in global energy confinement. These simplified transport models predict the same behavior of the global energy confinement time from L- to H-mode as the baseline transport model for both PDX and ASDEX.

Thus while the experiments can be fit by the baseline transport model which includes much that might be attractive from its basis in theoretical plasma physics, it is important to emphasize that the agreement is largely model independent. There is not enough evidence from these experiments to require profile factors in transport models, nor is it yet definite that a sum of several diffusivities is required to describe the ohmic, L-mode, and H-mode confinement regimes. When these models are tested against experiments at a wider variety of plasma parameters, it may become possible to distinguish between these and other plasma transport models.

7.5 Connection with theory

Our baseline model was chosen on the basis of broad empirical and theoretical constraints in addition to fitting the two detailed data sets presented here. It is interesting to recast this model in terms of variables which include theoretically appropriate dimensionless variables. Derivative models such as $\chi_e \propto n_e^{+1} T_e^{-1/2}$ may actually be very complicated when cast in terms of such variables. Evidently, the description of derivative models as "simpler" refers only to the appearance of the formulas when cast in empirical variables; it is not meant to imply these models are simpler in the context of any particular theoretical model. We therefore concentrate here only on the baseline model.

We choose the following dimensionless parameters appropriate to circular plasmas: an approximate $\varepsilon\beta_p \equiv \beta_{th} q^2/\varepsilon$ (where β_{th} is the local ratio of thermal plasma pressure to toroidal magnetic pressure), $\nu_{e*} = qR\nu_e/(\varepsilon^{3/2}\, v_{the})$ (where $\nu_e = 4(2\pi) n_e \lambda_* e^4/(3m_e{}^{1/2} T_e{}^{3/2})$, $\lambda_* = 24 - \ell n[n_*{}^{1/2}/T_*(\mathrm{eV})]$, and $v_{the} = (2T_e/m_e)^{1/2}$), and $\delta = \rho_H/r$ (where $\rho_H = v_{thH}/\Omega_H = (2T_i/m_H)^{1/2}/[eB/(m_H c)]$ is the proton toroidal gyroradius). Motivated by the theory of drift and kinetic ballooning modes, we express the dimensions of χ_e in terms of

$$\chi_H = \rho_H^2\, v_{thH}/R\ . \tag{13}$$

Eqs. (8) and (12) then become

$$\chi_{aux} = 0.06\ \chi_H\ \delta^{-1.1} (\varepsilon\beta_p)^{0.6} \nu_{e*}{}^{0.3} \varepsilon^{1.3} q^{0.9} \left(1 + \frac{n_i T_i}{n_e T_e}\right)^{0.9} \left(\frac{T_e}{T_i}\right)^{1.0} |\lambda_p|\,|\lambda_q|^{-2} \tag{14}$$

$$\chi_o = 0.04\ \chi_H \delta^{0.3} (\varepsilon\beta_p)^{-1.3} \nu_{e*}{}^{0.5} \varepsilon^{0.7} q^{1.9} \left(1 + \frac{n_i T_i}{n_e T_e}\right)^{1.3} \left(\frac{T_e}{T_i}\right)^{1.6} Z_{eff}{}^{0.25}. \qquad (15)$$

This form of χ_{aux} reflects the underlying physical motivation: turbulence is presumably driven by unfavorable curvature dependent on $\varepsilon\beta_p$ and $|\lambda_p|$, has a structure dependent on δ, and can be weakly affected by collisionality. Our expression for the χ_o contribution, dominant at low $\varepsilon\beta_p$, exhibits the suppression of the drift mode branch expected at high $\varepsilon\beta_p$ [10]. As the other scalings seen in Eq. (15) are not readily interpretable, this simple power law [Eq. (12)] for χ_o must therefore be regarded as an empirical formula, which is one possible expression for the combined kinetic and fluid effects dominant at low $\varepsilon\beta_p$.

Note the absence of (λ_{Debye}/r) in Eqs. (14) and (15) for χ_{aux} and χ_o. This absence is a reflection of the fact that the local transport coefficients obey the Kadomtsev-Connor-Taylor constraint for a collisional high-β plasma [18,19]. Note also that the uncertainty in all of the scaling exponents is at least ±0.2. There is therefore considerable room for remolding the above model into a more theoretically acceptable form for testing against the data sets.

8. CONCLUSIONS

There are two major conclusions of this work. First, a semiempirical model based on OH- and L-mode confinement scalings can reproduce the evolution of total stored energy in the H-mode as can several related models. No abrupt changes in plasma diffusivities are necessarily required at the L → H transition to reproduce the global energy confinement transition. Second, the results from this model are remarkably sensitive to the energy of incoming neutrals. Changing this energy in response to computed changes in the divertor temperature in the PDX case resulted in a significantly better fit to the evolution of the stored energy. These concepts and the data presented here should be useful in further studies of plasma transport in tokamaks.

ACKNOWLEDGMENTS

Members of the ASDEX and PDX experimental teams and the authors of BALDUR [15] provided invaluable help. We are particularly indebted to J. Strachan for providing the neutron emission data, M. Bell for $\beta(t)$, R. Fonck and K. Jaehnig for $T_i(t)$, and to G. Becker, R. Goldston, S. Kaye, K. McGuire, M. Petravic, and D. Post for many useful discussions, and also to D. Darrow, D. K. Owens, G. Schmidt, other members of the PDX group, and members of the ASDEX team.

This work was supported by the U. S. Department of Energy Contract No. DE-AC02-76-CHO-3073.

APPENDIX: Computational Method

Here we describe details in the scrape-off model and the core-plasma transport model used in this paper.

The poloidally averaged scrape-off particle loss time was $\tau_\parallel = Mv_s/L_\parallel$ where $v_s = [(T_i + T_e)/\bar{m}_i]^{1/2}$, $\bar{m}_i$ is the mean ion mass, and $L_\parallel$ is the half-length of an "open" magnetic field line. We estimated $L_\parallel = 2 \times 10^3$ cm at $r = 40.4 \pm 0.4$ cm and $L_\parallel = 1.2 \times 10^3$ cm for $r > 40.8$ cm. This local variation in $L_\parallel$ reflects the logarithmic singularity in $q(r)$ near the separatrix location $r = r_{sep} = 40$ cm. Differences between the PDX and ASDEX magnetic geometry were ignored for simplicity, since these differences are smaller than the uncertainty in the model used to describe the scrapeoff. The magnetic shear is corrected for this singularity using an approximate fit to MHD equilibrium calculations, $|\lambda_q| = (r/q_{cyl})\partial q_{cyl}/\partial r + 0.1/[0.01 + |q_{cyl} - q_{cyl}(r_{sep})|]$ where q_{cyl} is the safety factor computed with our equivalent circle model. The other small effects of this singularity were neglected.

The divertor temperature, T_{div}, was computed from the energy balance along magnetic field lines,

$$Q_{div} - W_{div} = 5\Gamma_{div}T_{div} + q_{\parallel e} , \tag{A1}$$

where $Q_{div} = 2(\lambda_i + \lambda_e)\Gamma_{div}T_{div}$ relates the heat flux lost through the sheath to specified effective sheath constants $\lambda_i = 1$ and $\lambda_e = 3$ [7,26], $W_{div} = \alpha\Gamma_{div}E$ is the radiative energy loss in the divertor throat, $\Gamma_{div} = n_{div}(2T_{div}/\bar{m}_i)^{1/2}$ is the sonic flow particle flux density to the divertor plate, α is the divertor reionization fraction defined in Sec. 2, $E = -60$ eV is the energy loss per ionization, $\Gamma_1 = \Gamma_{div}(1 - \alpha)$ relates the electron particle flux density Γ_1 from the main chamber to that at the divertor plate,

$$q_{\parallel e} = \min\left[n_e v_{the}\left(T_e - T_{div}\right),\ \kappa_{\parallel e}\left(T_e - T_{div}\right)/L_\parallel\right] , \qquad \text{(A2)}$$

is the flux-limited electron energy flow from the main plasma chamber, $v_{the} = (2T_{div}/m_e)^{1/2}$ is the electron thermal velocity, and $\kappa_{\parallel e}\left(Z_{eff}, T_b\right)$ the parallel electron thermal conduction coefficient evaluated at T_{div}. To compute the parallel energy losses for the scrapeoff in Eq. (1) we take $Q_e = q_{\parallel e} + 2.9\ \Gamma_1 (3/2)\ T_e$ and $Q_i = (3/2)(n_i/n_e)\ \Gamma_1 T_i$.

A rough scaling of neoclassical ion heat conduction with Z_{eff} was accomplished by setting $\chi_i^{CH} = \Sigma\ \chi_a^{CH}$ with the sum over all thermal plasma ions. Here

$$\chi_a^{CH} = \frac{n_a}{n_i} Z_{eff} A_a^{1/2} \frac{K_2(\nu_{*a})}{K_2(\nu_{*H})} \chi_H^{CH} ,$$

where χ_H^{CH} and $K_2(\nu_{*H})$ are the formulas of Chang and Hinton for a proton plasma and $K_2(\nu_{*a})$ is computed from the formula for K_2 of Chang and Hinton with the substitution $\nu_{*H} \rightarrow \nu_{*a} = \langle Z^2\rangle_a\ \nu_{*H}$. Here $Z_{eff} = \Sigma\ n_a\ \langle Z^2\rangle_a/n_e$, A_a is the atomic mass of species a, and $\langle Z^2\rangle_a$ is the coronal equilibrium mean square charge of species a.

A limit on the particle and electron thermal diffusion coefficients was set using the transformations

$$D_a \rightarrow \frac{2\ D_a D_B}{D_a + 2D_B} , \qquad \text{(A3)}$$

$$\chi_e \rightarrow \frac{2\ \chi_e \chi_B}{\chi_e + 2\ \chi_B} ,$$

where $D_B = cT_e/(16eB)$ and $\chi_B = 1.5\ D_B$. Impurities were added to PDX by launching neutrals inward from the separatrix with an energy of 50 eV and computing ionization with the appropriate cross section. For each oxygen and ion ionization there was a local electron energy loss of 3 keV and 5 keV, respectively. The anomalous impurity pinch was omitted in the scrapeoff. The χ_q terms were also omitted from D_a when computing the anomalous velocity $v_a = -D_a \partial \ell n n_e/\partial r$ to avoid excess pinching on axis. The thermal friction term in the neoclassical impurity transport is subject to considerable theoretical uncertainty. Following Rogister <u>et al.</u> [35] the thermal friction was therefore omitted. To give a reasonable minimum of $Z_{eff} = 1.2$ without detailed transport modeling of the negligible impurity levels in ASDEX and the ohmic phase of PDX, 0.67% carbon was included uniformly without associated radiative losses.

The fast ion contribution to the toroidal current was computed in a cylindrical model of fast ion deceleration. Corrections for electron drag on the beam-driven current in ASDEX included neoclassical effects [15,39]. The maximum net beam-driven current in ASDEX was 89 kA, at t = 1.18 s. For the perpendicular injection geometry in PDX, the beam-driven current is negligible and was neglected. The bootstrap current is of uncertain magnitude and was also neglected.

For PDX, the toroidal current was initiated at t = 0.15 s at 200 kA with current density $J \propto T_e^{-3/2}$, using $T_e = 0.328\ [1 - (r/50\ \text{cm})^{3.2}]^{2.2}$ keV. The current was ramped to 250 kA at t = 0.22 s and thereafter as in Fig. 3. For ASDEX, we ramped the current up to 375 kA as for PDX and then let the profile relax to an ohmic equilibrium for 0.4 s and the density profile relax at $\bar{n}_e = 4.1 \times 10^{13} \text{cm}^{-3}$ for 0.2 s before commencing beam injection. The ASDEX simulation had 10% hydrogen ions before injection, rising to 29% at t = 1.2 s due to beam fueling. The absorbing wall at r = 50 cm in PDX had to be moved to r = 45 cm in the ASDEX simulation to avoid numerical problems associated with a simulated hydrogen ion density of $n_H < 10^{10} cm^{-3}$ beyond r = 45 cm.

The BALDUR input data files for the PDX and ASDEX simulations can be accessed through the U.S. NMFECC computer network in files HAT459 and HAS048, respectively in filem area 4121; adequate comments are included in these files to access BALDUR version baldp19c-p17m-p09a and supporting files for reproducing or modifying these simulations.

REFERENCES

[1] WAGNER, F., BECKER, G., BEHRINGER, K., CAMPBELL, D., EBERHAGEN, A., *et al.*, in *Proceedings of the Ninth International Conference on Plasma Physics and Controlled Nuclear Fusion Research*, Vol. 1, 43, IAEA, Baltimore, 1983.

[2] WAGNER, F., BECKER, G., BEHRINGER, K., CAMPBELL, D., EBERHAGEN, A., *et al.*, Phys. Rev. Lett. *49*, (1982) 1408.

[3] KAYE, S.M., BELL, M., BOL, K., BOYD, D., BRAU, K., *et al.*, J. Nucl. Mater. *121* (1984) 115.

[4] OHYABU, N. *et al.*, in Proceedings of the IEEE International Conference on Plasma Science, San Diego, CA, 1983.

[5] OWENS, D. K., KAYE, S. M., FONCK, R. J., SCHMIDT, G. L., J. Nucl. Mater. *121* (1984) 29.

[6] WAGNER, F., BEHRINGER, K., CAMPBELL, D., EBERHAGEN, A., FUSSMANN, G., *et al.*, "Variation of the Particle Confinement During Neutral Injection into ASDEX Divertor Plasmas," Max Planck Institut für Plasmaphysik Report No. IPP-III/78 (1982).

[7] LANGER, W.D. and SINGER, C.E., "Two-Chamber Model for Divertors with Plasma Recycling," Princeton Plasma Physics Laboratory Report No. PPPL-2160 (1984); IEEE Transaction in Plasma Physics (in press).

[8] SINGER, C.E., "Understanding the H-mode," Princeton Plasma Physics Laboratory Report No. PPPL-TM-392 (1983).

[9] FONCK, R.J., BEIRSDORFER, P., BELL, M., BOL, K., BORD, D., *et al.*, H-Mode Studies in PDX, Fourth International Symposium on Heating in Toroidal Plasmas, Rome, March 21, 1984, Princeton Plasma Physics Laboratory Report No. PPPL-2118 (1984); Bull. Am. Phys. Soc. *28* (1983) 1052.

[10] REWOLDT, G., TANG, W. M., CHANCE, M. S., Phys. Fluids 25 (1982) 480.

[11] HASSAM, A. B., DRAKE, J. F., Phys. Fluids 26 (1983) 133.

[12] CARRERAS, B. A., DIAMOND, P. H., MURAKAMI, M., DUNLAP, J. L., BELL, J. D., et al., Phys. Rev. Lett. 50 (1983) 503.

[13] HINTON, F. L., HAZELTINE, R. D., Rev. Mod. Phys. 48 (1976) 239.

[14] SINGER, C. E., "Semiempirical Transport in Tokamaks," J. Fusion Energy 3, (1983) 231.

[15] SINGER, C. E., POST, D., MIKKELSEN, D., REDI, M., MC KENNEY, A., et al., Comp. Phys. Comm. (in press).

[16] DÜCHS, D. F., POST, D. E., RUTHERFORD, P. H., Nucl. Fusion 17 (1977) 565.

[17] HAWRYLUK, R. J., "An Empirical Approach to Tokamak Transport," Physics of Plasma Close to Thermonuclear Conditions, edited by B. Coppi et al., CEC Internal Document DUR-FU-BRU-XII/476180, Brussels (1980) Vol. 1, p. 19.

[18] KADOMTSEV, B. B., Fiz. Plazmy 1 (1975) 531 (Sov. J. Plasma Phys. JETP 1, (1975) 295).

[19] CONNOR, J. W., TAYLOR, J. B., Nucl. Fusion 17 (1977) 1047.

[20] PFEIFFER, W. W. and WALTZ, R. E., Nucl. Fusion 19 (1979) 51.

[21] POST, D. E., GOLDSTON, R. J., GRIMM, R. C., HAWRYLUK, R. J., in Proceedings of the Seventh International Conference on Plasma Physics and Controlled Nuclear Fusion Research, Vol. 1, 471, IAEA, Innsbruck, 1978.

[22] MIKKELSEN, D. R., "The Effects of Sawteeth on Energy Confinement in Ohmically Heated TFTR Discharges," in Proceedings of the TFTR/JET INTOR Workshop on Plasma Transport in Tokamaks (Princeton, N.J., July 9-10, 1984), Princeton Plasma Physics Laboratory Report PPPL-2182 (1984).

[23] JOHNSON, D., BELL, M., BITTER, M., BOL, K., BRAU, K., et al., in Proceedings of the Ninth International Conference on Plasma Physics and Controlled Nuclear Fusion Research, Vol. 1, 27, IAEA, Baltimore, 1983.

[24] NAGAMI, N. and the JAERI Team, OVERSKEI, D. and the GA Team, in Proceedings of the Ninth International Conference on Plasma Physics and Controlled Nuclear Fusion Research, Vol. 1, 27, IAEA, Baltimore, 1983.

[25] MURAKAMI, M., BATES, S. C., BELL, J. D., BUSH, C. E., CARNEVALI, A., et al., in Proceedings of the Ninth International Conference on Plasma Physics and Controlled Nuclear Fusion Research, Vol. 1, 57, IAEA, Baltimore, 1983.

[26] LANGER, W. D., SINGER, C. E., Bull. Am. Phys. Soc. 28 (1983) 1173.

[27] FREEMAN, R.L., JONES, E.M., "Atomic Collision Processes in Plasma Physics Experiments," Culham Laboratory Report No. UKAE CLM-R-137 (1974).

[28] HOWE, H., J. Vac. Sci. Technol. A1 (1983) 1435.

[29] SINGER, C. E. "New Recycling Model for Light Ions and Atoms Below 70 eV," Princeton Plasma Physics Laboratory Report No. PPPL-2102 (1985); J. Vac. Soc. A (in press); "Plasma-Wall Interaction at Low Particle Energy," Princeton Plasma Physics Laboratory, Applied Physics Division Report No. 29 (1984).

[30] ROBINSON, M.T., J. Nucl. Mater. 103/104 (1981) 525.

[31] CHANG, C. S., HINTON, F. L., Phys. Fluids 25 (1982) 1493.

[32] WARE, A., Bull. Am. Phys. Soc. 28 (1983) 1136.

[33] POST, D. E., JENSEN, R. V., TARTER, C. B., GRASSBERGER, W. H., and LOKKE, W. A., At. Data Nucl. Data Tables 20 (1977) 397.

[34] FONCK, R. J., HULSE, R. A., Phys. Rev. Lett. 52 (1984) 530.

[35] ROGISTER, A., and HASSELBERG, G., Nucl. Fusion 23 (1983) 1455.

[36] STRACHAN, J. et al., Nucl. Fusion 22 (1982) 1145.

[37] GOLDSTON, R. J., "Diagnostic Techniques for Magnetically Confined Plasmas II: Magnetic and Electric Measurements, Charge Exchange Diagnostics, Particle Beam Diagnostics, and Fusion Product Measurements," Princeton

Plasma Physics Laboratory Report No. PPPL-1924 (1982).

[38] BECKER, R. G., CAMPBELL, D., EBERHAGEN, A., GEHRE, D., GERNHARDT, J., Nucl. Fusion 23 (1983) 1293.

[39] SINGER, C. E., "Prediction of Neutral Beam Driven Current in PDX," Princeton Plasma Physics Laboratory Report No. PPPL-TM-318 (1978).

[40] TOWNER, H. H., GOLDSTON, R. J., BELL, M. G., DAVIS, S., Bull Am. Phys. Soc. 27 (1982) 1049.

[41] REDI, M., SINGER, C. E., MIKKELSEN, D.R., SEIDL, F.G.P, and LANGER, W.D, "H-Mode Simulations," in Proceedings of the TFTR/JET INTOR Workshop on Plasma Transport in Tokamaks (Princeton, N.J., July 9-10, 1984) Princeton Plasma Physics Laboratory Report PPPL-2182 (1984).

[42] BELL, M. G., FONCK, R. J., GREK, B., JAEHNIG, K. P., et al., J. Nucl. Mater. 121 (1984) 132.

[43] NAGAMI, M., et al., Proceedings of the Eighth European Physics Society, (Aachen, 1983).

[44] GOLDSTON, R., KAYE, S., DAVIS, S., BELL, M., BITTER, M., et al., "Confinement Studies with Neutral Beam Injection on PDX and PLT," in Proceedings of the Third Joint Varenna-Grenoble International Symposium on Heating in Toroidal Plasma (Grenoble, 1982).

TABLE 1. Confinement Times

Model	#1	#2	#3	#4
Description	Baseline	No. λ Factors	χ_o Only	$\chi_n \propto n_e^{-1} T_e^{-1/2}$
ASDEX - τ_E(msec)				
time(s), mode				
1.10(OH)	75	57	59	34
1.15(L)	45	50	35	34
1.2(H)	51	61	42	39
PDX - τ_E(msec)				
time(s), mode				
0.29(OH)	18	18	11	10
0.37(L)	16	20	10	13
0.48(L)	18	23	14	16
0.60(H)	39	43	35	31

FIGURE CAPTIONS

FIG. 1. Poloidal flux contours in the single-null PDX H-mode plasma, showing the approximate locations of the bolometers, divertor probe, divertor H_α chord, midplane interferometer, Thomson scattering, electron cyclotron emission diagnostics, and spectroscopy.

FIG. 2. Poloidal flux contours in the double-null ASDEX H-mode plasma showing interferometer chords, Thomson scattering, electron cyclotron emission, and charge-exchange geometry.

FIG. 3. Midplane line-average density $\bar{n}_e = \int n_e d\ell/(80\ \mathrm{cm})$ from PDX shot 61650 (digitized curve) and current from TRANSP code [14] Run 2302 (smooth curve labeled I_p) and from BALDUR code, simulation HAT459 (smooth curve and straight line segments). Injected beam power ramping was simulated by stepping from 1.1 MW at t = 0.29 sec to 2.2 MW at t = 0.31 sec. The experimental gas puffing rate was constant at 20-30 torr-liters/sec (1.4-2.1 × 10^{21} deuterons/sec) during neutral injection.

FIG. 4. Z_{eff} from visible Bremsstrahlung (which measures a centrally weighted $\bar{Z}_{eff} = \int Z_{eff}\, n_e^2\, T_e^{1/2}/\int n_e^2 T_e^{1/2} d\ell$ integrated across the midplane where $Z_{eff} = \Sigma\ n_a Z_a^2/n_e$) and from loop voltage measurements (assuming neoclassical resistivity; dashed curve) for PDX shots from the run date on which the profiles in Fig. 7b and Fig. 8b were taken (25 May 1983, four days after PDX shot 61650), and $\bar{Z}_{eff}$ from simulation (solid curve).

FIG. 5. Bolometer signals averaged from PDX shots 61498, 61522, 61526, 61532, 61533 (dashed curves [42]) compared to simulation (solid curves). Simulated bolometer signal includes thermal charge exchange, impurity radiation, and fast neutrals from charge exchange with circulating

beam ions, assuming 25% of the fast ions escape from the plasma and the remainder are redeposited locally [39]. (a) radially integrated profiles and (b) twice the lower half-plasma radiation from closed flux surfaces.

FIG. 6. Neutron emission rate from PDX shot 61650 during neutral beam injection, showing effects of fishbone oscillations.

FIG. 7. Electron density from simulation and Thomson scattering for (a) PDX shots 61643-61663 at t = 0.49 s (with L → H transitions at 0.50-0.54 s), (b) PDX shots 61960-61973 at t = 0.48 s (with L → H transitions at 0.47-0.48 s) and (c) PDX shots 61494, 61495, and 61499 (core plasma) and 61494-61516 (inset) at t = 0.58 s (with L → H transitions at t = 0.52±0.05 s). Error bars indicate the variance of shot-to-shot differences. The major radius is R = 140 + Δ ± r where the Shafranov shift, $\Delta = (3 + 5.6\ \beta_p)(1 - r^2/r_{scr}^2)$, is taken from the TRANSP code RUN 2302. Inset solid points with vertical crosses show data from the edge-plasma Thomson scattering system, with horizontal error bars comparable to the uncertainty in location of the separatrix from (a) PDX shots 61643-61663, (b) PDX shots 61960-61973, (c) PDX shots 61494, 61495, and 61499 (core plasma) and 61494-61516 (inset).

FIG. 8. Electron temperature profiles from Thomson scattering versus major radius (vertical bars and crossed dots) and simulation (dashed lines) as in Fig. 7. Solid dots show data from electron cyclotron emission from Fig. 9.

FIG. 9. Time evolution of electron temperature at various major radii, R, in PDX from electron cyclotron emission calibrated to TVTS in an ohmic discharge, versus simulation, and ion temperature from spectroscopic

measurements (averages from R = 142 cm and R = 152 cm). Error bars indicate shot-to-shot variance in Thomson scattering data from similar discharges. There is a random $\gtrsim \pm 25$ eV uncertainty due to residual error after correcting for neutron heating of the detectors.

FIG. 10. Measurements and simulation for β_T and $\Lambda = \beta_p + \ell_i/2$ where ℓ_i is the internal inductance. Simulation results (smooth curves) are corrected for beam ion anisotropy [37] in order to predict the same quantities measured by the diamagnetic loop (for β_T, calibrated to simulation at the solid dot) and equilibrium field (for Λ) and processed by the CAAN [40] analysis code (wiggly curves) for PDX shot 61650. The lower solid curves show the effects of altering baseline simulation HAT336 with beam power reduced by fishbone losses as described in the text. The dashed smooth curve is for constant neutral energy as described in the text.

FIG. 11. $\bar{n}_e$ as in Fig. 3, and at 20 cm above the midplane, for ASDEX shot 8475 (upper digitized curves, showing a sawtooth event at the L+H transition) and from simulation HAS048 (smooth curves); H_α emission (cf. Fig. 2) in the divertor (lower digitized curve). Injected beam power ramping was simulated by stepping from 2.14 MW at t = 1.106 sec to 2.85 MW at t = 1.146 sec.

FIG. 12. Electron density for ASDEX at (a) t = 1 s, during ohmic heating, (b) at t = 1.15 s, just before the H-mode transition, and (c) at t = 1.20 s, 0.05 s after the H-mode transition (except that Fig. 7c shows data and simulation at t = 1.225 sec), with simulation (solid curve). The abscissa is the midplane half-width of flux surfaces with correction for the Shafranov shift from a plasma equilibrium calculation at each time point. Solid dots are from the YAG laser and open circles from

the ruby laser Thomson scattering with typical errors indicated by vertical lines.

FIG. 13. Electron and ion temperatures for ASDEX as in Fig. 12. Open circles are T_e from electron cyclotron emission, triangles are from the edge Thomson scattering system, small dots with and without uncrossed vertical lines are from the core-plasma Thomson scattering system. Squares are the central ion temperature inferred from neutron emission (with two values plotted in Fig.14c representing error limits due to uncertainty in fractions of hydrogen and of nonthermal deuterons), and solid dots (with and without crossed vertical lines) are charge-exchange ion temperatures. Solid curves indicate electron temperatures and dashed curves ion temperatures from simulation.

FIG. 14. β_T and Λ, as in Fig. 10, from simulation (solid curves, corrected for beam anisotropy [37]) and from ASDEX shot 8475 (dashed curves).

FIG. 15. χ_{aux}, density gradient contribution χ_{OH} to χ_q, and final Bohm-limited χ_e versus minor radius for (a) PDX simulation HAT336 at t = 0.29 s (OH), t = 0.49 s (L) and t = 0.60 s (H), and (b) ASDEX simulation HAT049 at t = 1.10 s (OH), t = 1.15 s (L), and t = 1.20 s (H).

FIG. 16. Simulated T_e profiles versus data as in Figs. 8 and 13 with transport models described in Table 1.

#84P0469

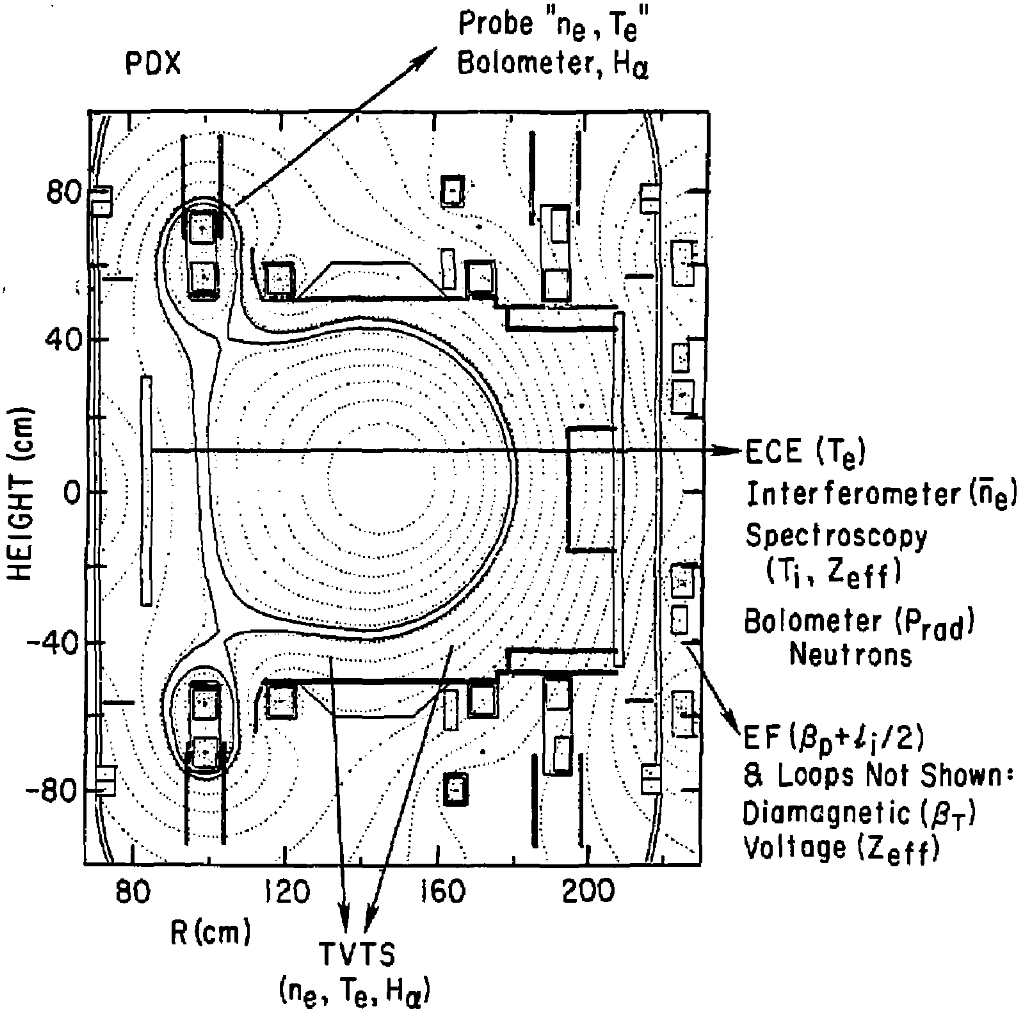

Fig. 1

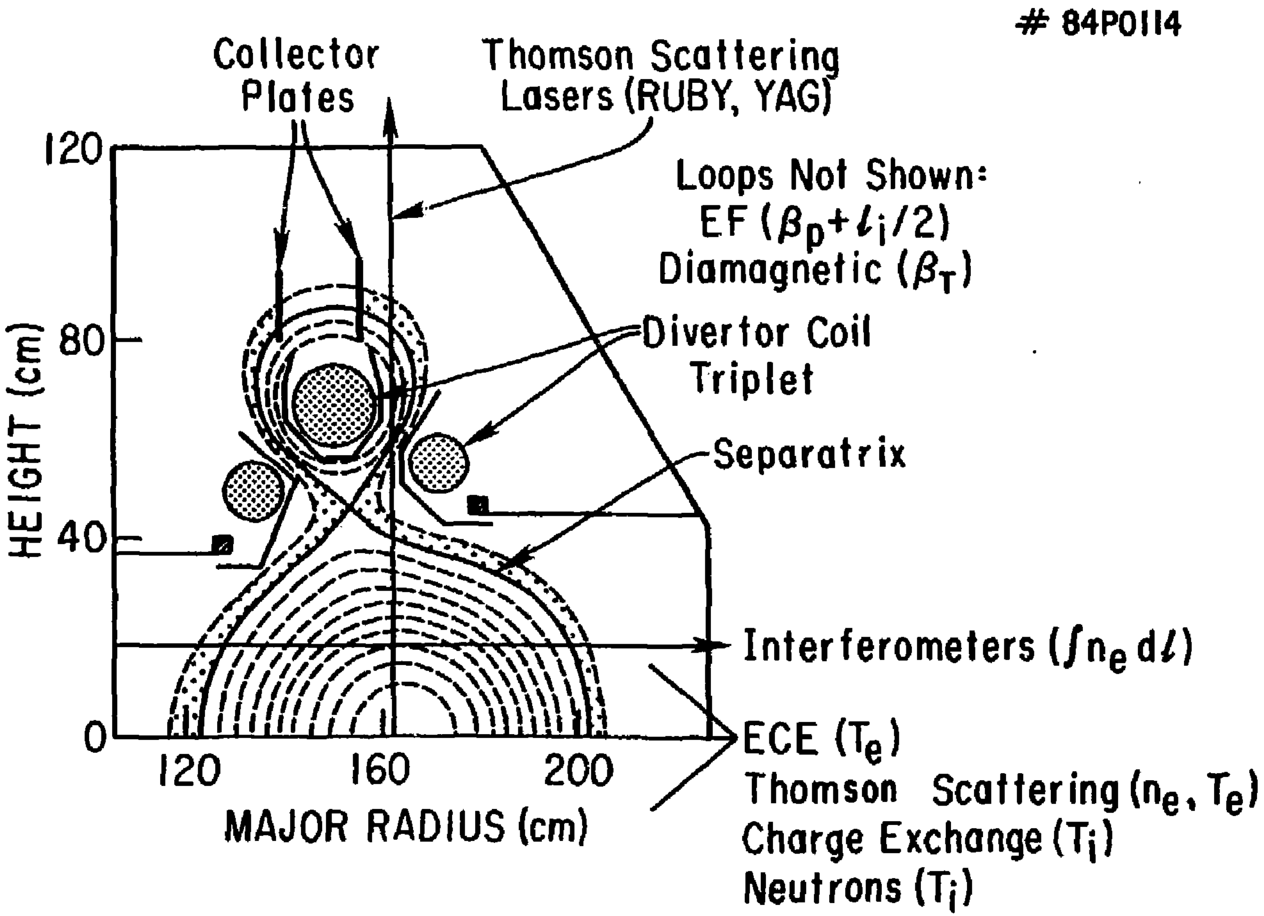
84P0114
Collector Plates
Thomson Scattering Lasers (RUBY, YAG)
Loops Not Shown:
EF ($\beta_p + \ell_i/2$)
Diamagnetic (β_T)
Divertor Coil Triplet
Separatrix
Interferometers ($\int n_e \, d\ell$)
ECE (T_e)
Thomson Scattering (n_e, T_e)
Charge Exchange (T_i)
Neutrons (T_i)
HEIGHT (cm)
120
80
40
0
120
160
200
MAJOR RADIUS (cm)

Fig. 2

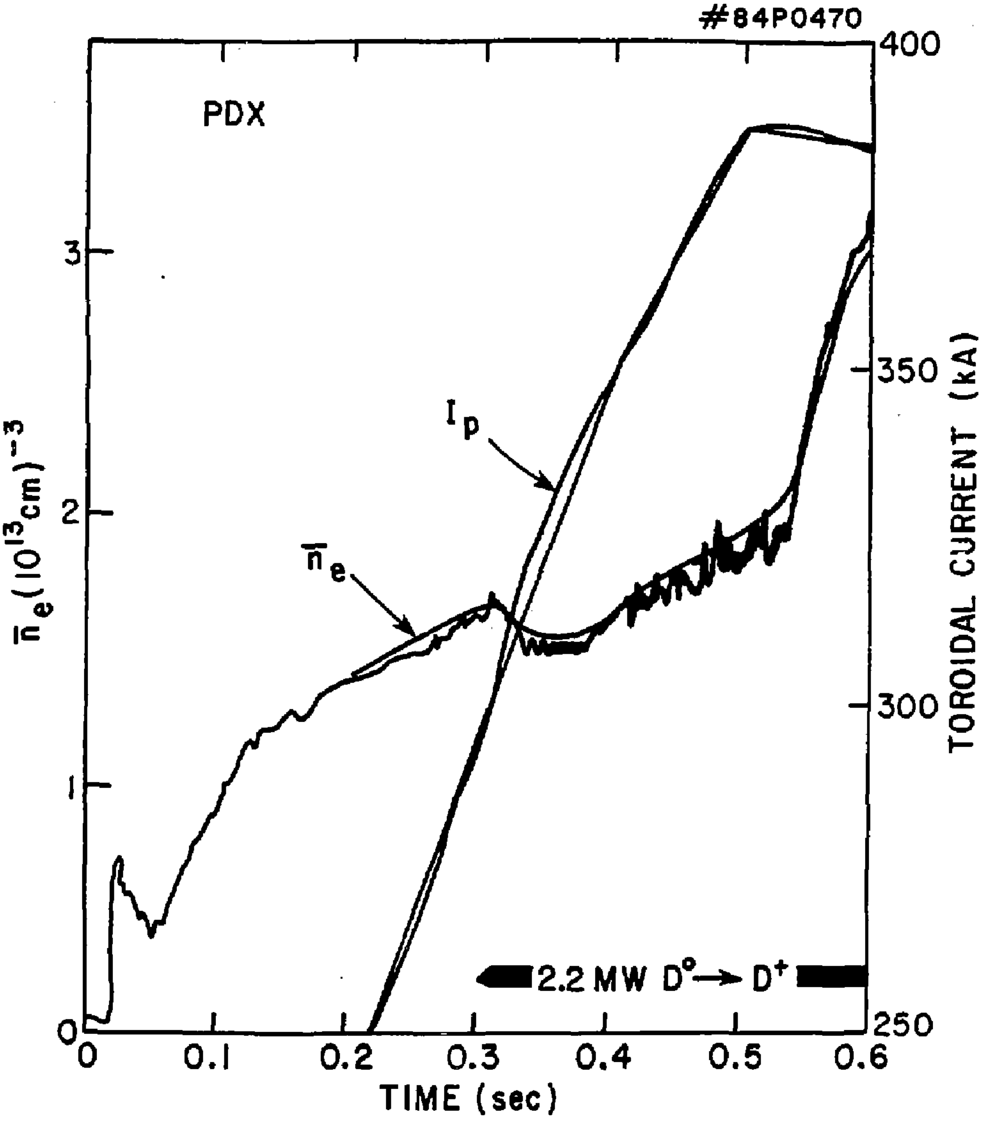
#84P0470
PDX
I_p
$\bar{n}_e$
2.2 MW $D^{\circ} \rightarrow D^{+}$
$\bar{n}_e (10^{13} cm)^{-3}$
0
1
2
3
TOROIDAL CURRENT (kA)
250
300
350
400
TIME (sec)
0
0.1
0.2
0.3
0.4
0.5
0.6

Fig. 3

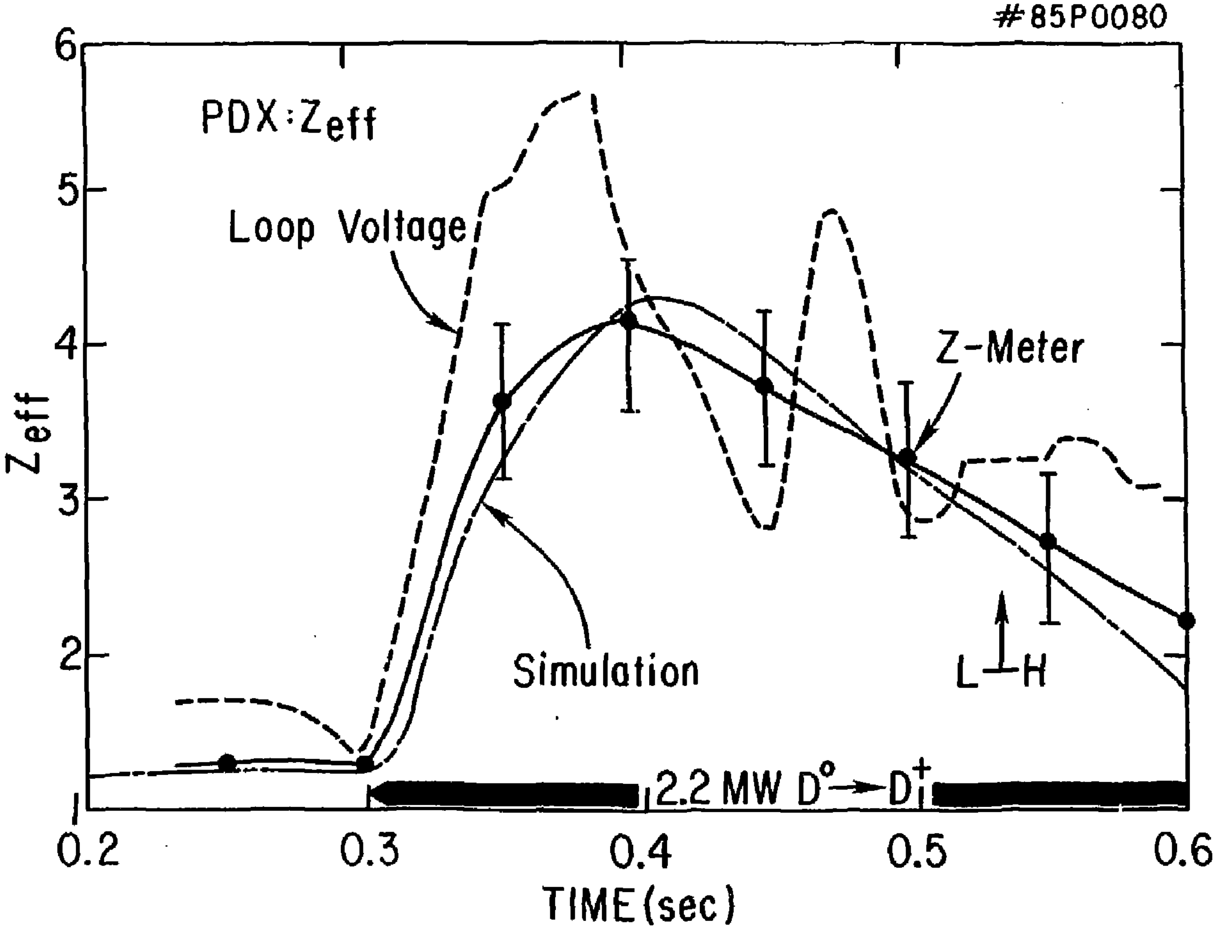
#85P0080
PDX: Z_{eff}
Loop Voltage
Z-Meter
Simulation
L H
2.2 MW $D^o \rightarrow D_i^+$
Z_{eff}
6
5
4
3
2
1
0.2
0.3
0.4
0.5
0.6
TIME (sec)

Fig. 4

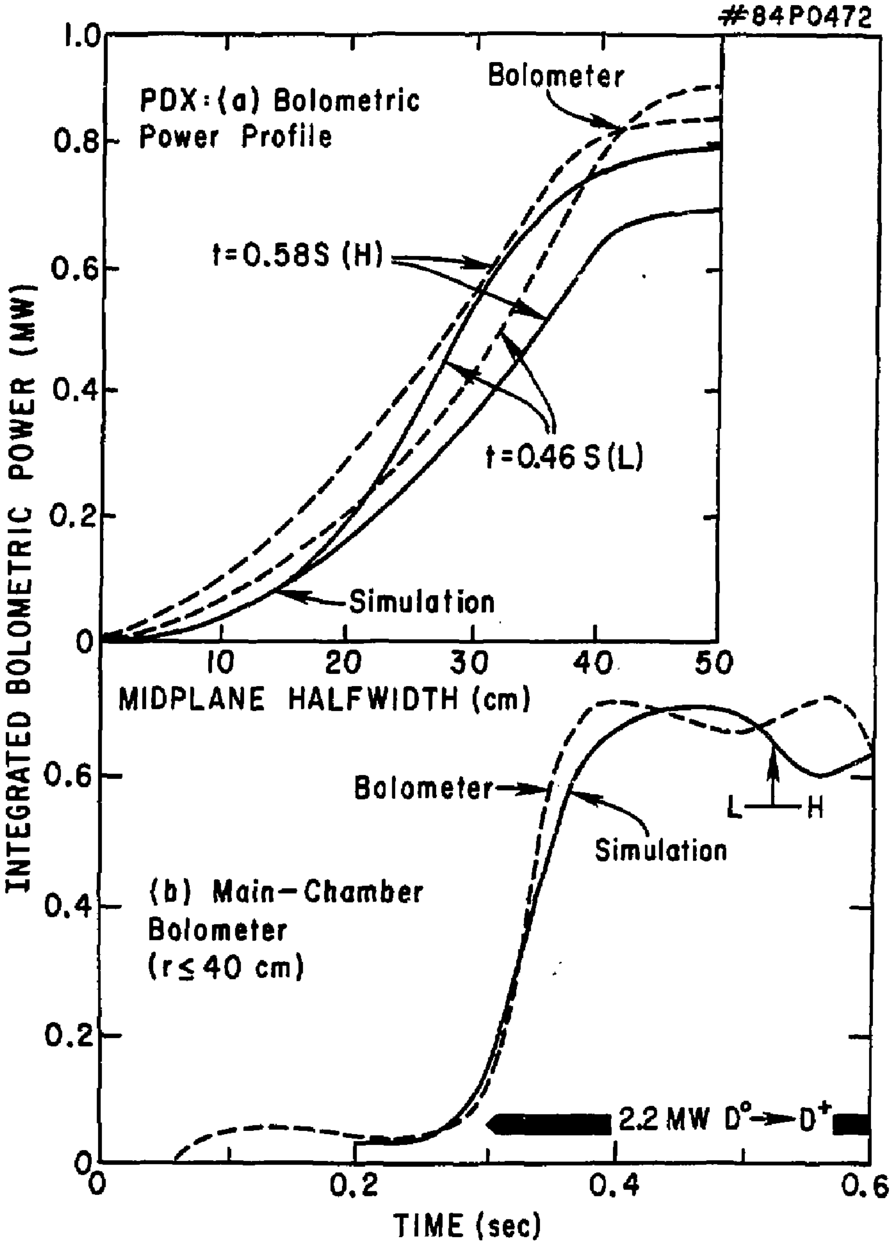
#84P0472
INTEGRATED BOLOMETRIC POWER (MW)
1.0
0.8
0.6
0.4
0.2
0
PDX: (a) Bolometric Power Profile
Bolometer
t=0.58S (H)
t=0.46 S (L)
Simulation
10
20
30
40
50
MIDPLANE HALFWIDTH (cm)
0.6
0.4
0.2
0
Bolometer
Simulation
L
H
(b) Main-Chamber Bolometer (r≤40 cm)
2.2 MW D°→D⁺
0
0.2
0.4
0.6
TIME (sec)

Fig. 5

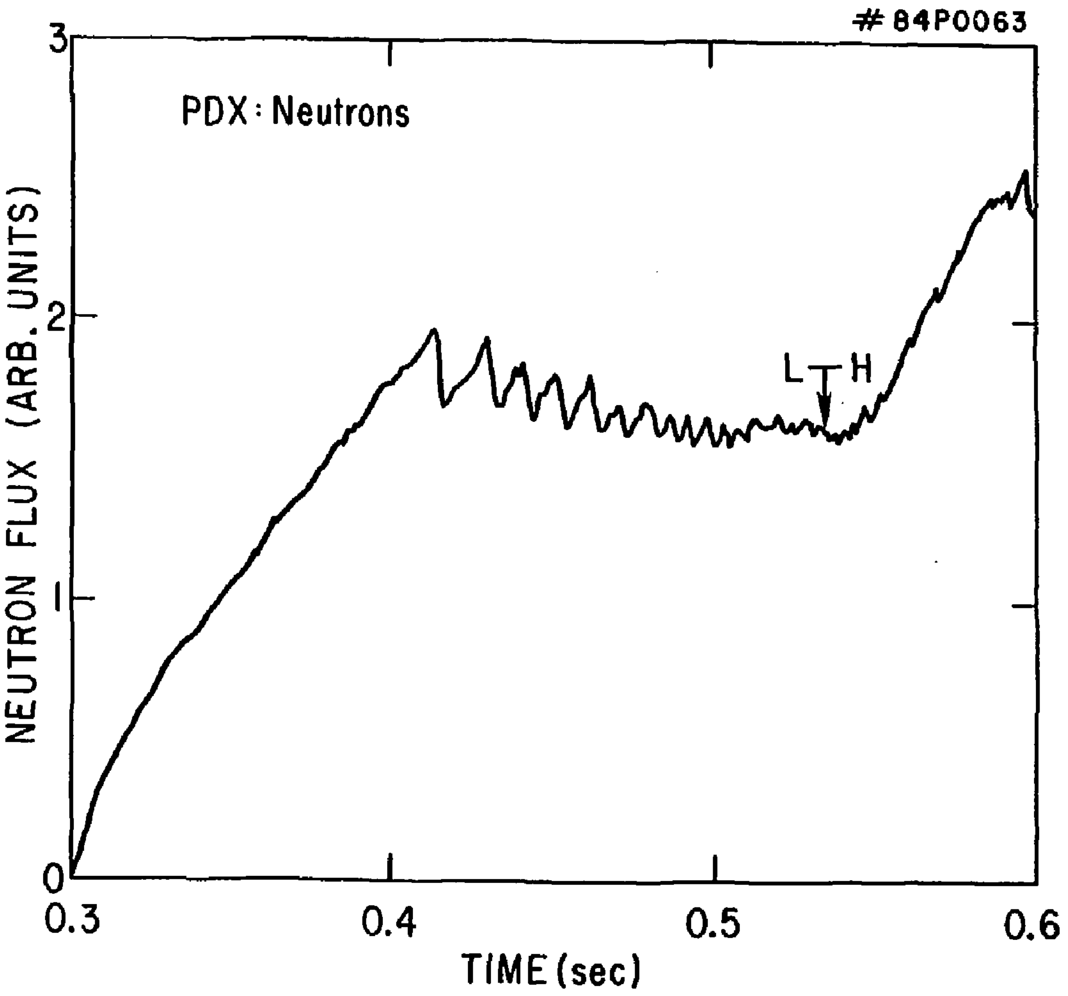
#84P0063
PDX: Neutrons
NEUTRON FLUX (ARB. UNITS)
0
1
2
3
0.3
0.4
0.5
0.6
TIME (sec)
L
H

Fig. 6

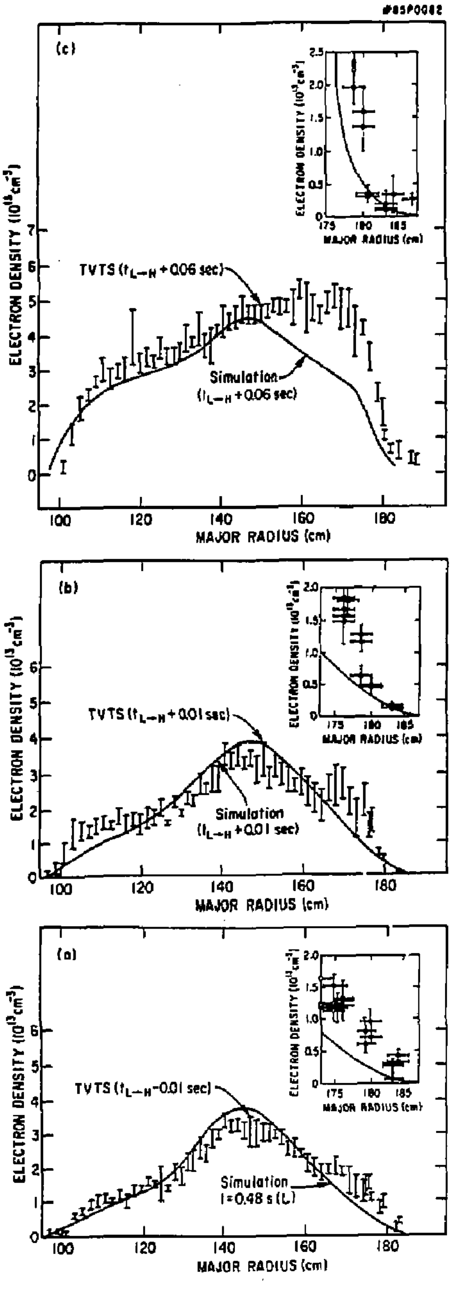
#85P0082
(c)
ELECTRON DENSITY (10^{13}cm^{-3})
TVTS ($t_{L\to H}$+0.06 sec)
Simulation ($t_{L\to H}$+0.06 sec)
MAJOR RADIUS (cm)
(b)
TVTS ($t_{L\to H}$+0.01 sec)
Simulation ($t_{L\to H}$+0.01 sec)
(a)
TVTS ($t_{L\to H}$-0.01 sec)
Simulation t=0.48 s (L)
0
1
2
3
4
5
6
7
100
120
140
160
180
175
185
0.5
1.0
1.5
2.0
2.5

Fig. 7

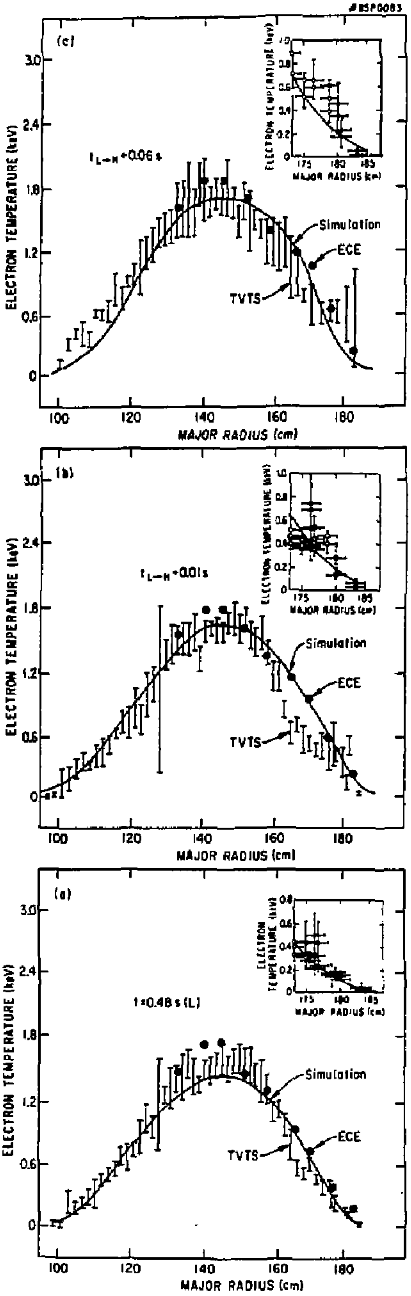
#85P0083
(c)
(b)
(a)
ELECTRON TEMPERATURE (keV)
0
0.6
1.2
1.8
2.4
3.0
t_L→H+0.06 s
t_L→H+0.01 s
t=0.48 s (L)
Simulation
ECE
TVTS
MAJOR RADIUS (cm)
100
120
140
160
180
175
180
185
0.2
0.4
0.6
0.8
1.0

Fig. 8

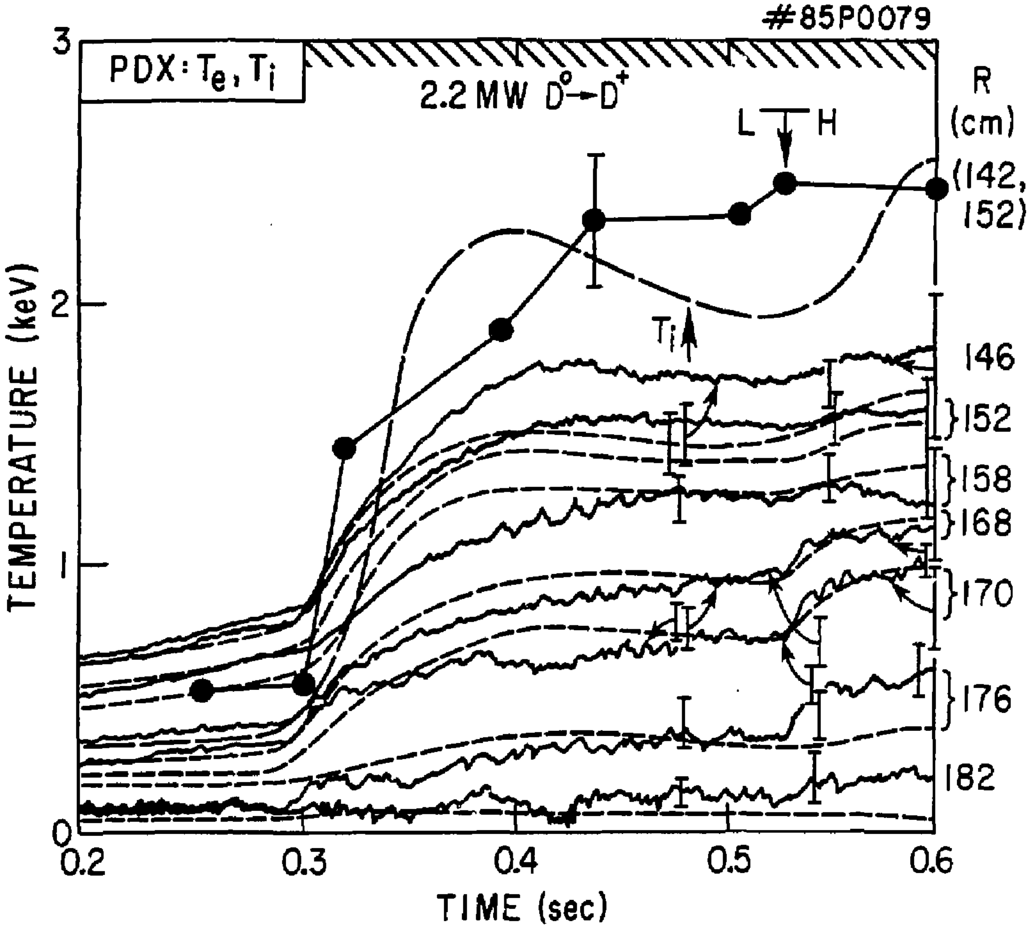
#85P0079
PDX: T_e, T_i
2.2 MW $D^o \to D^+$
L H
R (cm)
(142, 152)
T_i
146
152
158
168
170
176
182
TEMPERATURE (keV)
0
1
2
3
0.2
0.3
0.4
0.5
0.6
TIME (sec)

Fig. 9

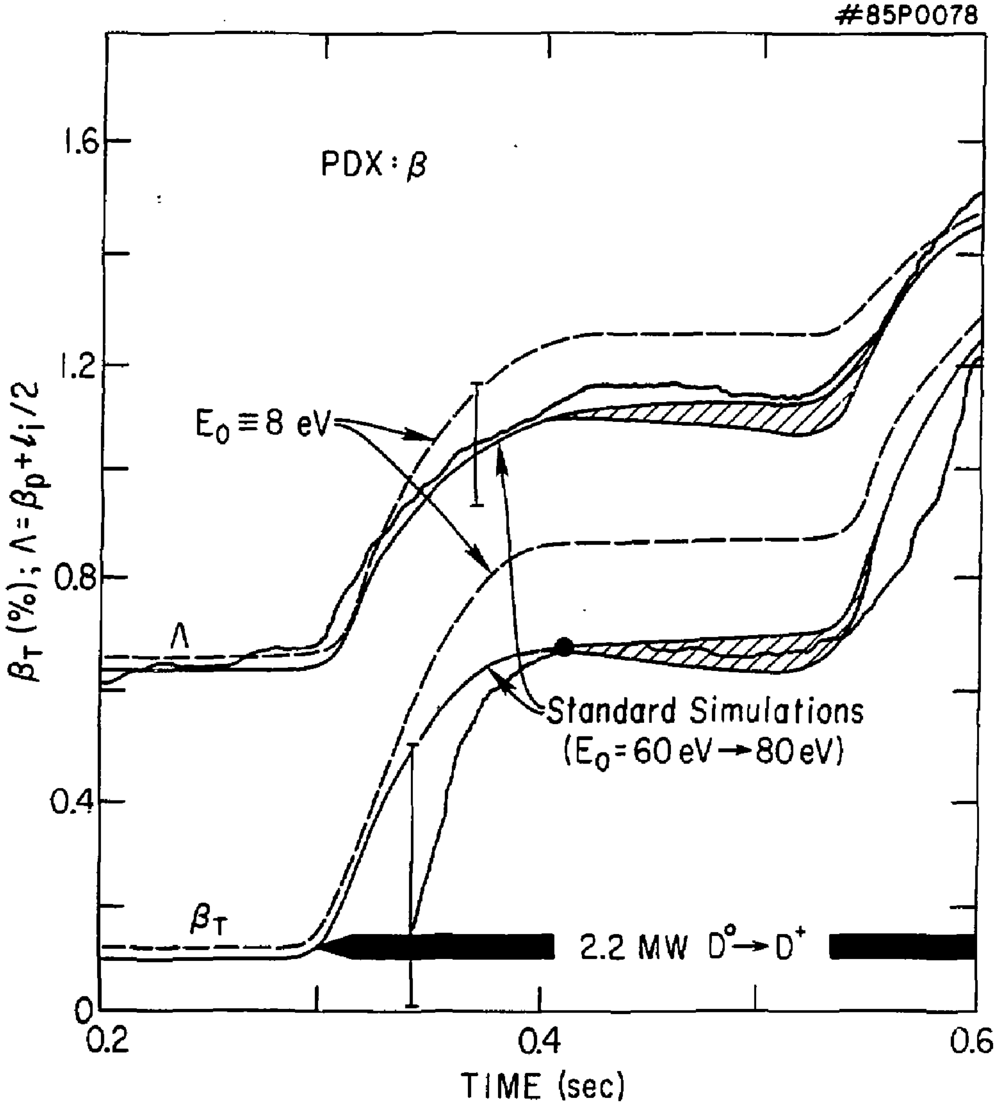
#85P0078
PDX : β
β_T (%); $\Lambda = \beta_p + \ell_i/2$
1.6
1.2
0.8
0.4
0
0.2
0.4
0.6
TIME (sec)
$E_0 \equiv 8$ eV
Λ
β_T
Standard Simulations
(E_0=60 eV → 80 eV)
2.2 MW $D^0 \rightarrow D^+$

Fig. 10

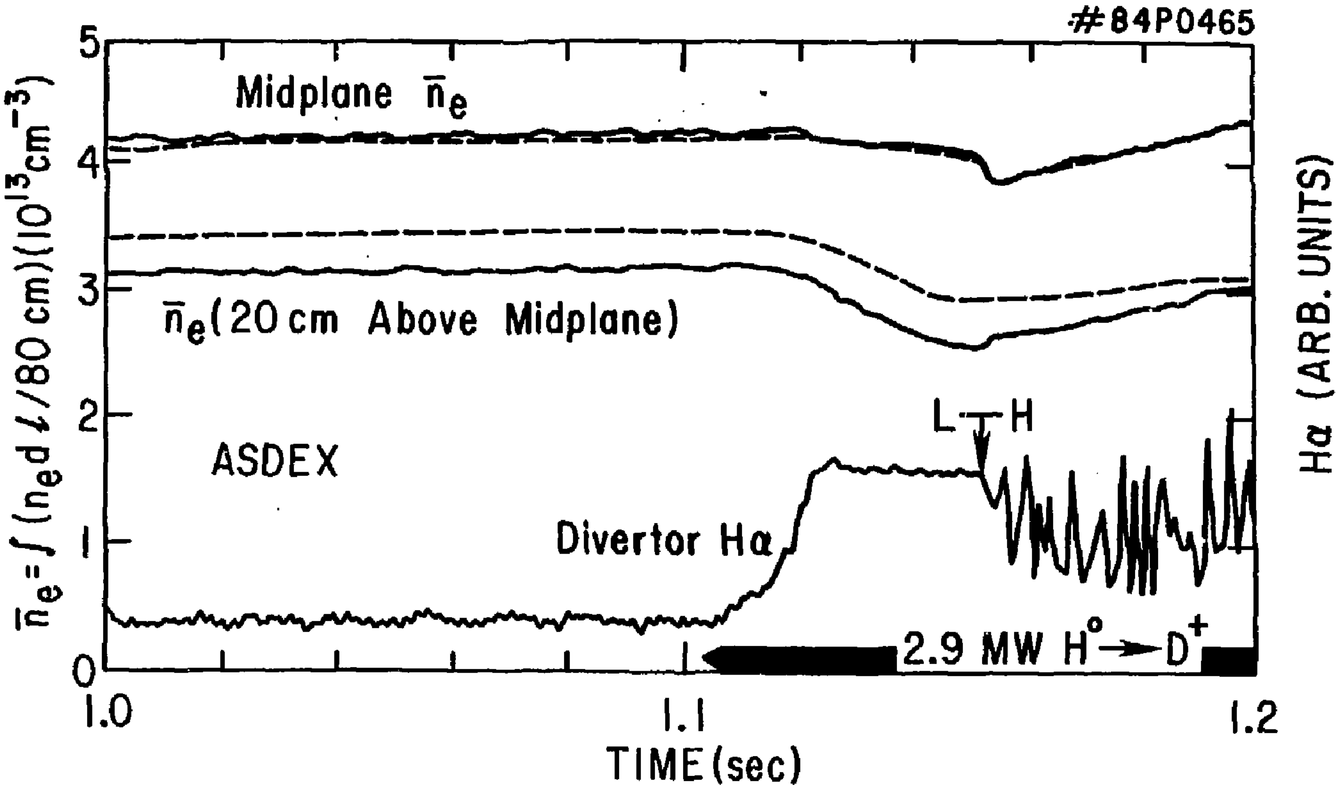
#84P0465
Midplane $\bar{n}_e$
$\bar{n}_e$(20 cm Above Midplane)
ASDEX
Divertor Hα
L→H
2.9 MW $H^o \rightarrow D^+$
$\bar{n}_e = \int (n_e d\ell/80\ cm)(10^{13} cm^{-3})$
Hα (ARB. UNITS)
TIME (sec)
0
1
2
3
4
5
1.0
1.1
1.2

Fig. 11

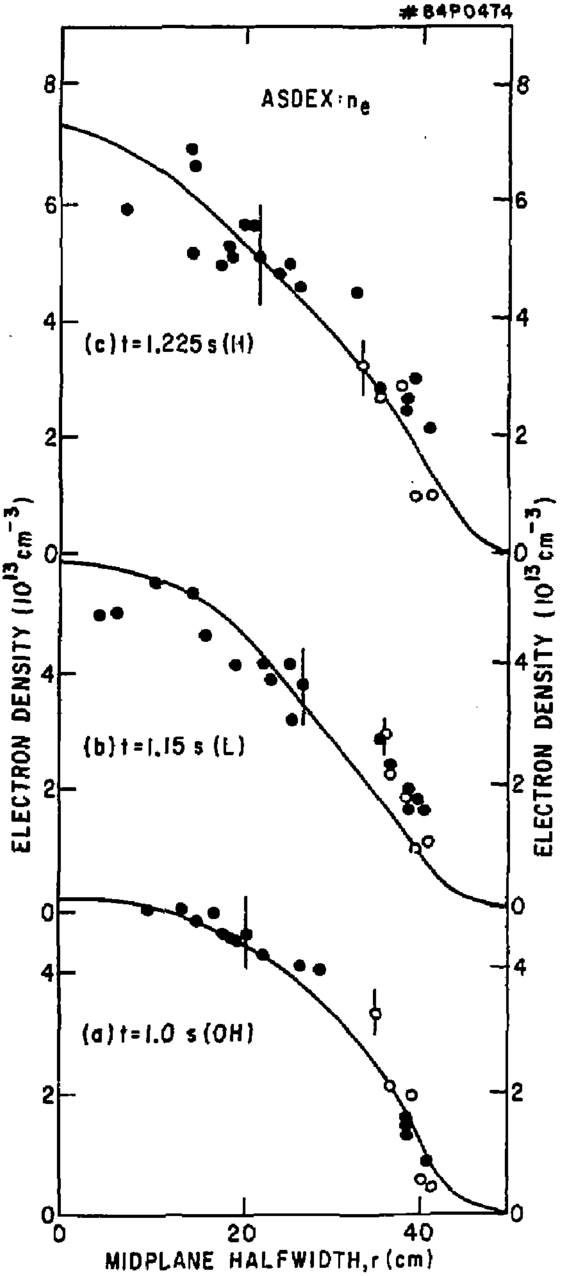
#84P0474
ASDEX: n_e
(c) t=1.225 s (H)
(b) t=1.15 s (L)
(a) t=1.0 s (OH)
ELECTRON DENSITY (10^{13} cm^{-3})
MIDPLANE HALFWIDTH, r (cm)
0
20
40
0
2
4
6
8

Fig. 12

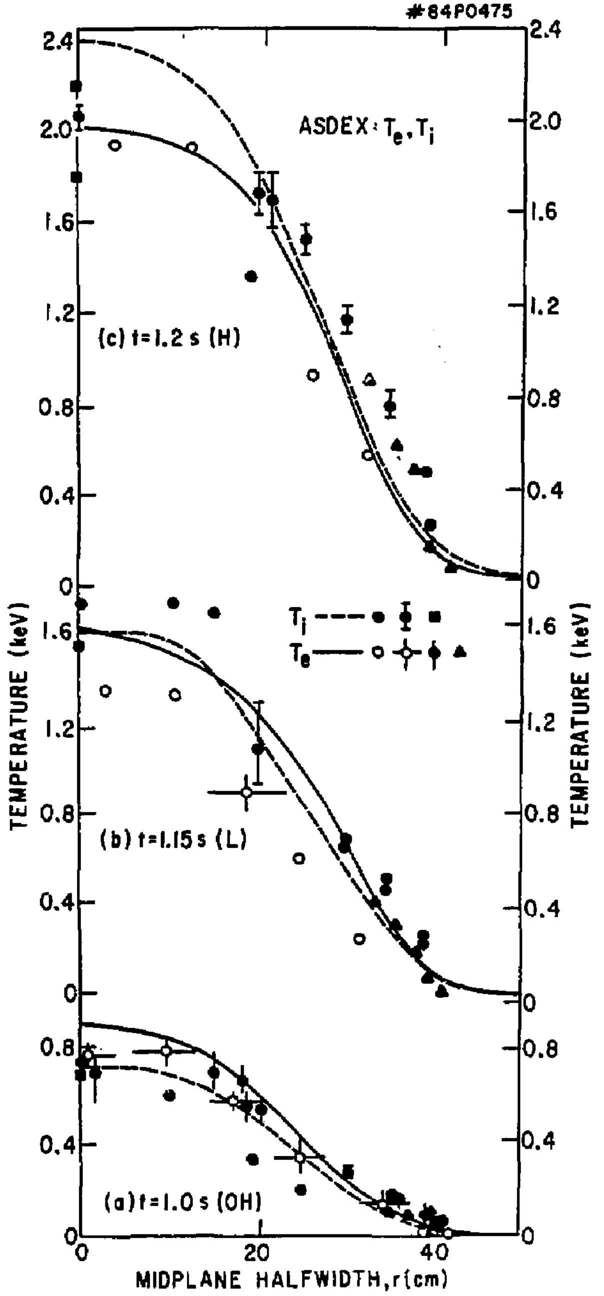
#84P0475
ASDEX: T_e, T_i
(c) t=1.2 s (H)
(b) t=1.15 s (L)
(a) t=1.0 s (OH)
T_i ----- ● ⫯ ■
T_e —— ○ ⌖ ⫯ ▲
TEMPERATURE (keV)
MIDPLANE HALFWIDTH, r (cm)
0
20
40
0
0.4
0.8
1.2
1.6
2.0
2.4

Fig. 13

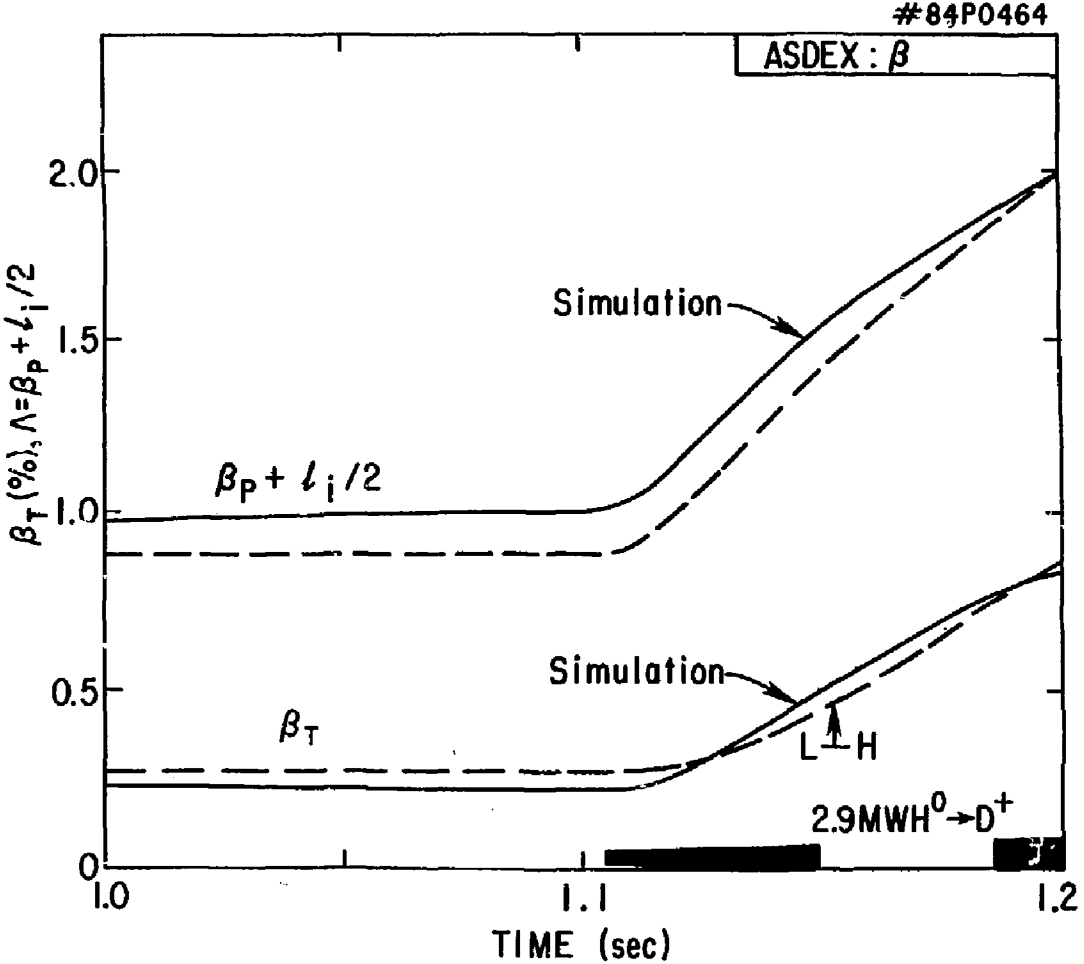
#84P0464
ASDEX : β
β_T (%), $\Lambda=\beta_P+\ell_i/2$
2.0
1.5
1.0
0.5
0
Simulation
$\beta_P+\ell_i/2$
Simulation
β_T
L H
2.9MWH$^0\rightarrow$D$^+$
1.0
1.1
1.2
TIME (sec)

Fig. 14

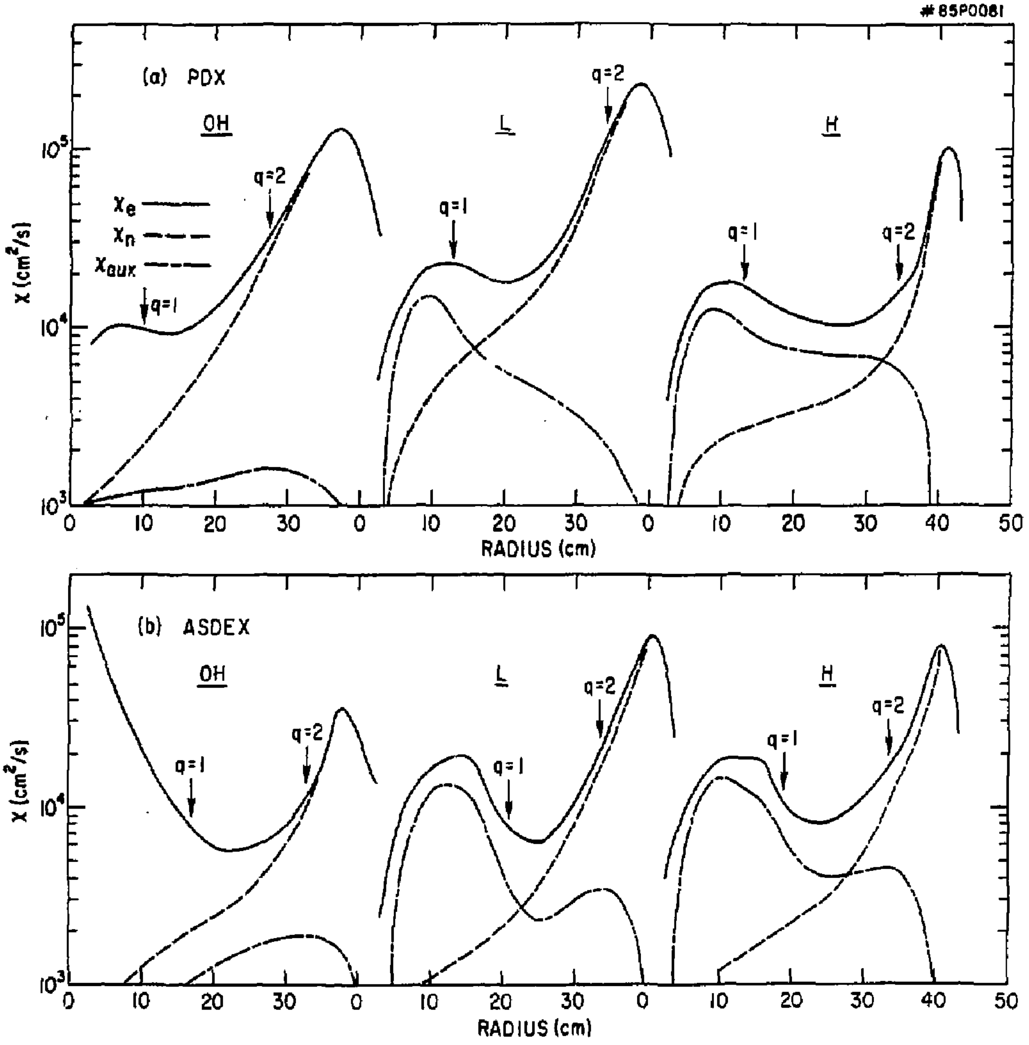
#85P0081
(a) PDX
OH
L
H
χ_e
χ_n
χ_{aux}
q=1
q=2
χ (cm^2/s)
10^3
10^4
10^5
0
10
20
30
40
50
RADIUS (cm)
(b) ASDEX

Fig. 15

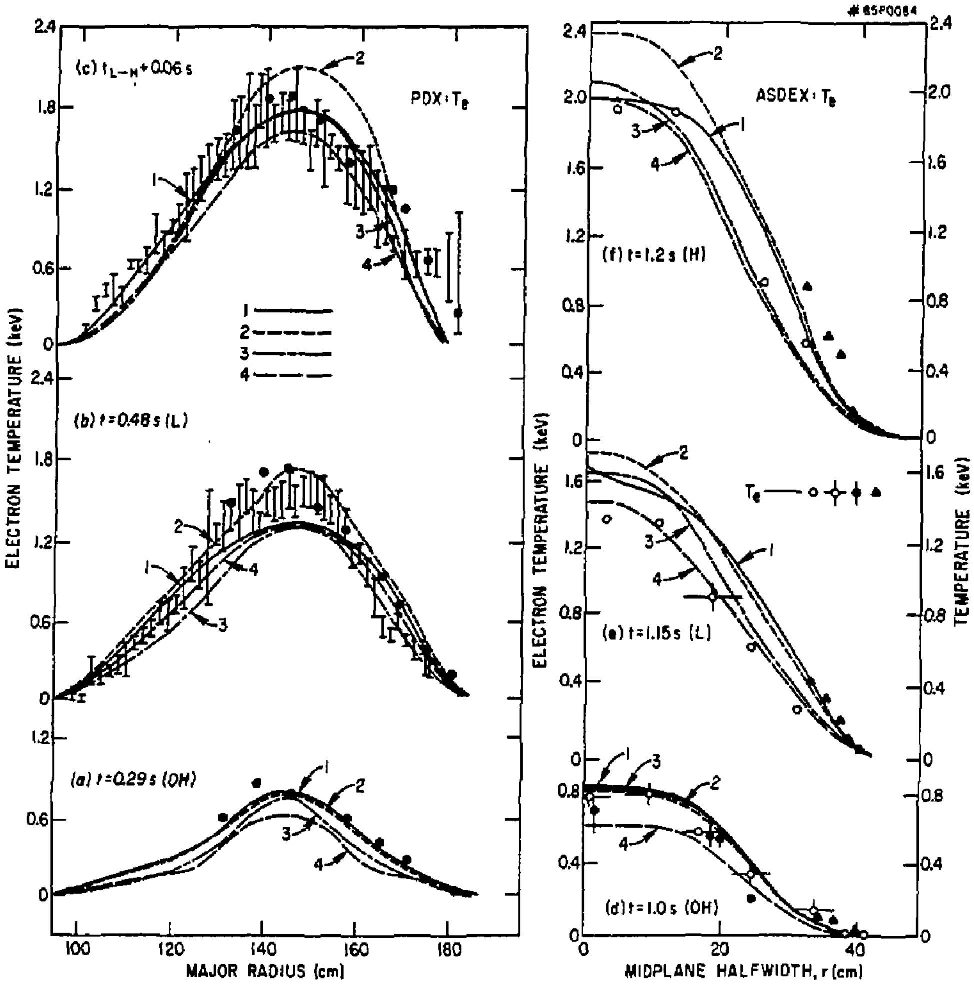

85P0084
PDX: T_e
(c) t_{L-H}+0.06 s
(b) t=0.48 s (L)
(a) t=0.29 s (OH)
1
2
3
4
ELECTRON TEMPERATURE (keV)
MAJOR RADIUS (cm)
100
120
140
160
180
0
0.6
1.2
1.8
2.4
ASDEX: T_e
(f) t=1.2 s (H)
(e) t=1.15 s (L)
(d) t=1.0 s (OH)
T_e
ELECTRON TEMPERATURE (keV)
TEMPERATURE (keV)
MIDPLANE HALFWIDTH, r (cm)
0
20
40
0.4
0.8
1.2
1.6
2.0
2.4

Fig. 16

EXTERNAL DISTRIBUTION IN ADDITION TO UC-20

Plasma Res Lab, Austra Nat'l Univ, AUSTRALIA
Dr. Frank J. Paoloni, Univ of Wollongong, AUSTRALIA
Prof. I.R. Jones, Flinders Univ., AUSTRALIA
Prof. M.H. Brennan, Univ Sydney, AUSTRALIA
Prof. F. Cap, Inst Theo Phys, AUSTRIA
Prof. Frank Verheest, Inst theoretische, BELGIUM
Dr. D. Palumbo, Dg XII Fusion Prog, BELGIUM
Ecole Royale Militaire, Lab de Phys Plasmas, BELGIUM
Dr. P.H. Sakanaka, Univ Estadual, BRAZIL
Dr. C.R. James, Univ of Alberta, CANADA
Prof. J. Teichmann, Univ of Montreal, CANADA
Dr. H.M. Skarsgard, Univ of Saskatchewan, CANADA
Prof. S.R. Sreenivasan, University of Calgary, CANADA
Prof. Tudor W. Johnston, INRS-Energie, CANADA
Dr. Hannes Barnard, Univ British Columbia, CANADA
Dr. M.P. Bachynski, MPB Technologies, Inc., CANADA
Chalk River, Nucl Lab, CANADA
Zhengwu Li, SW Inst Physics, CHINA
Library, Tsing Hua University, CHINA
Librarian, Institute of Physics, CHINA
Inst Plasma Phys, Academia Sinica, CHINA
Dr. Peter Lukac, Komenskeho Univ, CZECHOSLOVAKIA
The Librarian, Culham Laboratory, ENGLAND
Prof. Schatzman, Observatoire de Nice, FRANCE
J. Radet, CEN-BP6, FRANCE
AM Dupas Library, AM Dupas Library, FRANCE
Dr. Tom Mual, Academy Bibliographic, HONG KONG
Preprint Library, Cent Res Inst Phys, HUNGARY
Dr. S.K. Trehan, Panjab University, INDIA
Dr. Indra Mohan Lal Das, Banaras Hindu Univ, INDIA
Dr. L.K. Chavda, South Gujarat Univ, INDIA
Dr. R.K. Chhajlani, Vikram Univ. INDIA
Dr. B. Dasgupta, Saha Inst, INDIA
Dr. P. Kaw, Physical Research Lab, INDIA
Dr. Phillip Rosenau, Israel Inst Tech, ISRAEL
Prof. S. Cuperman, Tel Aviv University, ISRAEL
Prof. G. Rostagni, Univ Di Padova, ITALY
Librarian, Int'l Ctr Theo Phys, ITALY
Miss Clelia De Palo, Assoc EURATOM-ENEA, ITALY
Biblioteca, del CNR EURATOM, ITALY
Dr. H. Yamato, Toshiha Res & Dev, JAPAN
Direc. Dept. Lg. Tokamak Dev. JAERI, JAPAN
Prof. Nobuyuki Inoue, University of Tokyo, JAPAN
Research Info Center, Nagoya University, JAPAN
Prof. Kyoji Nishikawa, Univ of Hiroshima, JAPAN
Prof. Sigeru Mori, JAERI, JAPAN
Library, Kyoto University, JAPAN
Prof. Ichiro Kawakami, Nihon Univ, JAPAN
Prof. Satoshi Itoh, Kyushu University, JAPAN
Dr. D.I. Choi, Adv. Inst Sci & Tech, KOREA
Tech Info Division, KAERI, KOREA
Bibliotheek, Fom-Inst Voor Plasma, NETHERLANDS
Prof. B.S. Liley, University of Waikato, NEW ZEALAND
Prof. J.A.C. Cabral, Inst Superior Tecn, PORTUGAL
Dr. Octavian Petrus, ALI CUZA University, ROMANIA
Prof. M.A. Hellberg, University of Natal, SO AFRICA
Dr. Johan de Villiers, Plasma Physics, Nucor, SO AFRICA
Fusion Div. Library, JEN, SPAIN
Prof. Hans Wilhelmson, Chalmers Univ Tech, SWEDEN
Dr. Lennart Stenflo, University of UMEA, SWEDEN
Library, Royal Inst Tech, SWEDEN
Centre de Recherchesen, Ecole Polytech Fed, SWITZERLAND
Dr. V.T. Tolok, Kharkov Phys Tech Ins, USSR
Dr. D.D. Ryutov, Siberian Acad Sci, USSR
Dr. G.A. Eliseev, Kurchatov Institute, USSR
Dr. V.A. Glukhikh, Inst Electro-Physical, USSR
Institute Gen. Physics, USSR
Prof. T.J.M. Boyd, Univ College N Wales, WALES
Dr. K. Schindler, Ruhr Universitat, W. GERMANY
Nuclear Res Estab, Julich Ltd, W. GERMANY
Librarian, Max-Planck Institut, W. GERMANY
Bibliothek, Inst Plasmaforschung, W. GERMANY
Prof. R.K. Janev, Inst Phys, YUGOSLAVIA